AIAA Journal
Vol. 48, No. 12, December 2010

Large-Eddy Simulation of Plasma-Based Turbulent Boundary-Layer Separation Control

Donald P. Rizzetta[*] and Miguel R. Visbal[†]
U.S. Air Force Research Laboratory, Wright-Patterson Air Force Base, Ohio 45433-7512

DOI: 10.2514/1.J050014

Large-eddy simulations were carried out in order to numerically describe plasma-based control of turbulent boundary-layer separation. The configuration consisted of a flat-plate section, over which the boundary layer developed, followed by a curved convex rearward-facing ramp, corresponding to an experimental arrangement. A single dielectric-barrier-discharge plasma actuator was then employed to reduce the extent of the separated flow region. Solutions were obtained to the Navier–Stokes equations, which were augmented by source terms used to represent plasma-induced body forces imparted by the actuator on the fluid. A simple phenomenological model provided the electric field generated by the plasma, resulting in the body forces. The numerical method used a high-fidelity time-implicit scheme, employing domain decomposition in order to perform calculations on a parallel computing platform. Simulations were first conducted for an isolated actuator, which were used to optimize parameters inherent in the plasma model. Subsequent calculations were then carried out for the plate development section and for the plate/ramp combination, using both continuous and pulsed control. All simulations were compared with experimental measurements, which indicated that, although some deficiencies were apparent in the plasma model, they appeared to be adequate for use with large-eddy simulation in the exploration of plasma-based control for turbulent wall-bounded flows.

Nomenclature

A = plasma-force pulsing amplitude function
C_f = skin-friction coefficient
C_p = surface pressure coefficient
D_c = plasma scale parameter
$\boldsymbol{E}$ = nondimensional electric field vector
E = total specific energy
E_{k_z}, E_ω = nondimensional turbulent-kinetic-energy wave number and frequency spectra
E_r = reference electric-field magnitude
E_x, E_y, E_z = nondimensional components of the electric-field vector
e_c = electron charge, 1.6×10^{-19} C
$\boldsymbol{F}, \boldsymbol{G}, \boldsymbol{H}$ = inviscid vector fluxes
$\boldsymbol{F}_v, \boldsymbol{G}_v, \boldsymbol{H}_v$ = viscous vector fluxes
f = dimensional imposed actuator pulsing frequency, 20 Hz
$\mathcal{J}$ = Jacobian of the coordinate transformation
K = nondimensional turbulent kinetic energy
k_z = spanwise wave number
l = reference length, 1.0 m
M = Mach number
$\boldsymbol{Q}$ = vector of dependent variables
Pr = Prandtl number, 0.73 for air
p = nondimensional static pressure
q = nondimensional velocity magnitude, $\sqrt{u^2 + v^2}$
$\mathcal{Q}_i$ = components of the heat flux vector
q_c = nondimensional charge density
R = ramp radius of curvature
Re = reference Reynolds number, $\rho_\infty u_\infty l / \mu_\infty$
$\boldsymbol{S}$ = source vector
T = nondimensional static temperature
t = nondimensional time
t_d = portion of fundamental period over which pulsed actuator is active
t_p = nondimensional actuator fundamental pulsing period
U, V, W = contravariant velocity components
u, v, w = nondimensional Cartesian velocity components in the x, y, and z directions
u_1, u_2, u_3 = u, v, and w
x, y, z = nondimensional Cartesian coordinates in the streamwise, vertical, and spanwise directions
x_a = streamwise location of actuator covered-electrode trailing edge
x_r = streamwise location of ramp origin
x_1, x_2, x_3 = x, y, and z
y_w = vertical location of the solid wall
γ = specific heat ratio, 1.4 for air
$\Delta \boldsymbol{Q}$ = $\boldsymbol{Q}^{p+1} - \boldsymbol{Q}^p$
Δt = time-step size
$\Delta x, \Delta y, \Delta z$ = computational mesh sizes in streamwise, vertical, and spanwise directions
δ = nondimensional boundary-layer thickness
δ_{ij} = Kronecker delta function
$\delta_{\xi 2}, \delta_{\eta 2}, \delta_{\zeta 2}, \delta_{\xi 6}, \delta_{\eta 6}, \delta_{\zeta 6}$ = second-order and sixth-order finite-difference operators in ξ, η, and ζ
μ = nondimensional molecular viscosity coefficient
ξ, η, ζ = nondimensional body-fitted computational coordinates
$\xi_t, \xi_x, \xi_y, \xi_z, \eta_t, \eta_x, \eta_y, \eta_z, \zeta_t, \zeta_x, \zeta_y, \zeta_z$ = metric coefficients of the coordinate transformation
ρ = nondimensional fluid density
ρ_c = electron charge number density, $1 \times 10^{11}/\text{cm}^3$
τ_{ij} = components of the viscous stress tensor
ω = nondimensional imposed actuator pulsing frequency, lf/u_∞

Subscript

∞ = dimensional reference value

Presented as Paper 2009-4287 at the 39th AIAA Fluid Dynamics Conference, San Antonio, TX, 22–25 June 2009; received 18 June 2009; revision received 25 September 2009; accepted for publication 9 November 2009.

[*] Senior Research Aerospace Engineer, Computational Sciences Branch of the Aeronautical Sciences Division of the Air Vehicles Directorate. Associate Fellow AIAA.

[†] Technical Area Leader, Computational Sciences Branch of the Aeronautical Sciences Division of the Air Vehicles Directorate. Associate Fellow AIAA.

Superscripts

n = time level
p = subiteration level
^ = filtered value
− = time-mean quantity
+ = law-of-the-wall variable

I. Introduction

THE use of plasma-based actuators is currently being explored as a means of actively controlling a variety of diverse flow situations. As an alternative to more complex mechanical or pneumatic systems, such devices have no moving parts and relatively low power requirements, and they can operate over a broad range of actuation frequencies. These considerations have spawned a number of experimental investigations that include rotorcraft blade control [1], lift enhancement for stationary and oscillating airfoils [2–4], plasma flaps and slats [5], dynamic stall [6], tip clearances in turbine blades [7], landing gear and bluff-body flows [8,9], turbine-blade flowfields [10–14], and aerodynamic control of unmanned air vehicles [15]. Several related numerical computations have also been performed, in which modeling was typically used to represent plasma-induced body forces imparted by actuators on the fluid field. Such simulations have been carried out for the control of wall-bounded flows [16], wing sections [17], delta wings [18], low-pressure turbine blades [19,20], and cylinder flowfields [21].

Dielectric-barrier-discharge (DBD) plasma actuators typically operate in the low radio frequency range of 1–10 kHz. Although voltage amplitudes of 5–10 kV were applied to early actuator designs, more recent devices use much higher voltages [8,9], providing more control effectiveness. An overview of the design, optimization, and application of these actuators has been given by Corke and Post [12]. Experimental measurements indicate that time-averaged body forces generated by such DBD devices are the dominant mechanism for exerting control. Because of this, simple models that account for these forces may be effectively used in numerical calculations. This approach is particularly useful in the large-eddy simulation (LES) of complex turbulent flows, which places severe demands upon computational resources.

Although the aforementioned numerical simulations have indicated great potential for plasma-based actuators to effectively control various flow situations, there has often been an absence of comparison with corresponding experimental measurements. This has made it difficult to associate the numerically observed control benefits with specific actuator performance, especially because of the force models that were employed. It is the purpose of the present study to provide a more detailed comparison between numerical simulations and experimental investigations than has previously been possible.

The experiments of Schatzman and Thomas [22] considered the use of plasma actuators for flow control of turbulent boundary-layer separation that occurs in high-Reynolds-number aerodynamic flows. The primary configuration of interest consisted of a flat-plate section over which the boundary layer developed, followed by a curved convex rearward-facing ramp. Measurements were taken in the separated flow region, as well as on the developmental plate when the aft ramp was absent. In addition, data are also available for an isolated actuator in the absence of any external flow. This comprehensive set of experimental information enables direct comparisons with numerical simulations.

Computations were first performed for the isolated actuator, which was operated in both a continuous and pulsed manner. Comparisons with experimental data allowed optimization for the choice of parameters inherent in the plasma model. A LES was then carried out for the developmental plate, so that an equilibrium turbulent boundary layer corresponding to the experimental conditions could be achieved numerically. Solutions for the plate with both continuous and pulsed actuation were then obtained. Finally, simulations were conducted for the complete plate/ramp configuration. In the sections to follow, the governing equations, the empirical plasma model, the numerical method, and the LES approach are described. Details of the simulations are summarized, and numerical results are presented. Comparisons are made with available experimental data and with baseline flows for which no control was enforced.

II. Governing Equations

The governing fluid equations are taken as the unsteady three-dimensional compressible unfiltered Navier–Stokes equations. Although these computations are considered to be LESs, it will be subsequently explained why, unlike more traditional approaches, the unfiltered equations are solved. After introducing a curvilinear coordinate transformation to a body-fitted system, the equations are cast in the following nondimensional conservative form [23,24]:

$$\frac{\partial}{\partial t}\left(\frac{1}{\mathcal{J}}\boldsymbol{Q}\right)+\frac{\partial}{\partial\xi}\left(\boldsymbol{F}-\frac{1}{Re}\boldsymbol{F}_v\right)+\frac{\partial}{\partial\eta}\left(\boldsymbol{G}-\frac{1}{Re}\boldsymbol{G}_v\right)+\frac{\partial}{\partial\zeta}\left(\boldsymbol{H}-\frac{1}{Re}\boldsymbol{H}_v\right)=D_c q_c\boldsymbol{S} \tag{1}$$

Here, t is the time, ξ, η, and ζ are the computational coordinates, $\boldsymbol{Q}$ is the vector of dependent variables, $\boldsymbol{F}$, $\boldsymbol{G}$, and $\boldsymbol{H}$ are the inviscid flux vectors, $\boldsymbol{F}_v$, $\boldsymbol{G}_v$, and $\boldsymbol{H}_v$ are the viscous flux vectors, and $\boldsymbol{S}$ is the source vector representing the effect of plasma-induced body forces. The vector of dependent variables is given as

$$\boldsymbol{Q}=[\rho \quad \rho u \quad \rho v \quad \rho w \quad \rho E]^T \tag{2}$$

the vector fluxes are given by

$$\boldsymbol{F}=\frac{1}{\mathcal{J}}\begin{bmatrix}\rho U\\ \rho uU+\xi_x p\\ \rho vU+\xi_y p\\ \rho wU+\xi_z p\\ \rho EU+\xi_{x_i}u_i p\end{bmatrix},\qquad \boldsymbol{G}=\frac{1}{\mathcal{J}}\begin{bmatrix}\rho V\\ \rho uV+\eta_x p\\ \rho vV+\eta_y p\\ \rho wV+\eta_z p\\ \rho EV+\eta_{x_i}u_i p\end{bmatrix}$$

$$\boldsymbol{H}=\frac{1}{\mathcal{J}}\begin{bmatrix}\rho W\\ \rho uW+\zeta_x p\\ \rho vW+\zeta_y p\\ \rho wW+\zeta_z p\\ \rho EW+\zeta_{x_i}u_i p\end{bmatrix} \tag{3}$$

$$\boldsymbol{F}_v=\frac{1}{\mathcal{J}}\begin{bmatrix}0\\ \xi_{x_i}\tau_{i1}\\ \xi_{x_i}\tau_{i2}\\ \xi_{x_i}\tau_{i3}\\ \xi_{x_i}(u_j\tau_{ij}-\mathcal{Q}_i)\end{bmatrix},\qquad \boldsymbol{G}_v=\frac{1}{\mathcal{J}}\begin{bmatrix}0\\ \eta_{x_i}\tau_{i1}\\ \eta_{x_i}\tau_{i2}\\ \eta_{x_i}\tau_{i3}\\ \eta_{x_i}(u_j\tau_{ij}-\mathcal{Q}_i)\end{bmatrix}$$

$$\boldsymbol{H}_v=\frac{1}{\mathcal{J}}\begin{bmatrix}0\\ \zeta_{x_i}\tau_{i1}\\ \zeta_{x_i}\tau_{i2}\\ \zeta_{x_i}\tau_{i3}\\ \zeta_{x_i}(u_j\tau_{ij}-\mathcal{Q}_i)\end{bmatrix} \tag{4}$$

with the source term

$$\boldsymbol{S}=\frac{1}{\mathcal{J}}\begin{bmatrix}0\\ E_x\\ E_y\\ E_z\\ uE_x+vE_y+wE_z\end{bmatrix} \tag{5}$$

and

$$D_c=\frac{\rho_c e_c E_r l}{\rho_\infty u_\infty^2} \tag{6}$$

where

$$U=\xi_t+\xi_{x_i}u_i,\qquad V=\eta_t+\eta_{x_i}u_i,\qquad W=\zeta_t+\zeta_{x_i}u_i \tag{7}$$

$$E=\frac{T}{\gamma(\gamma-1)M_\infty^2}+\frac{1}{2}(u^2+v^2+w^2) \tag{8}$$

In the preceding expressions, u, v, and w are the Cartesian velocity components, ρ is the density, p is the pressure, and T is the temperature. All length scales have been nondimensionalized by the reference length l, and dependent variables have been normalized by their reference values, except for p, which has been nondimensionalized by $\rho_\infty u_\infty^2$. Components of the heat flux vector and the stress tensor are expressed as

$$\mathcal{Q}_i = -\left[\frac{1}{(\gamma-1)M_\infty^2}\right]\left(\frac{\mu}{Pr}\right)\frac{\partial \xi_j}{\partial x_i}\frac{\partial T}{\partial \xi_j} \tag{9}$$

$$\tau_{ij} = \mu\left(\frac{\partial \xi_k}{\partial x_j}\frac{\partial u_i}{\partial \xi_k} + \frac{\partial \xi_k}{\partial x_i}\frac{\partial u_j}{\partial \xi_k} - \frac{2}{3}\delta_{ij}\frac{\partial \xi_l}{\partial x_k}\frac{\partial u_k}{\partial \xi_l}\right) \tag{10}$$

The Sutherland law for the molecular viscosity coefficient μ and the perfect gas relationship

$$p = \frac{\rho T}{\gamma M_\infty^2} \tag{11}$$

were also employed, and Stokes' hypothesis for the bulk viscosity coefficient has been invoked.

III. Empirical Plasma Model

Many quantitative aspects of the fundamental processes governing plasma/fluid interactions remain unknown or computationally prohibitive, particularly for transitional and turbulent flows. These circumstances have given rise to the development of a wide spectrum of models, with varying degrees of sophistication, that may be employed for more practical simulations. Among the simplified methods focused specifically on discharge/fluid coupling is that of Roth et al. [25,26], who associated transfer of momentum from ions to neutral particles based upon the gradient of electric pressure. A more refined approach, suitable for coupling with fluid response, was an empirical model proposed by Shyy et al. [27], using separate estimates for the charge distribution and electric field. Known plasma physics parameters were linked to experimental data. This representation has been successfully employed for several previous simulations of plasma-controlled flows [16–21], and its basic formulation was also adopted in the present investigation.

A schematic representation of a typical single asymmetric DBD plasma actuator is depicted in Fig. 1a. (Note that the extent of the plasma region has been exaggerated in the figure.) The actuator consists of two electrodes that are separated by a dielectric insulator and mounted on a body surface. An alternating current voltage, in the 1–10 kHz frequency range, is applied to the electrodes, developing an electric field about the actuator. When the imposed voltage is sufficiently high, the dielectric produces a barrier discharge that weakly ionizes the surrounding gas. Momentum acquired by the resulting charged particles from the electric field is transferred to the primary neutral molecules by a combination of electrodynamic body forces and poorly understood complex collisional interactions. Because the bulk fluid cannot respond rapidly to the high-frequency alternating voltage, the dominant effect of actuation is to impose a time-mean electric field on the external flow. In the numerical simulation of control applications, the entire process may be modeled as a body force vector acting on the net fluid adjacent to the actuator, which produces a flow velocity.

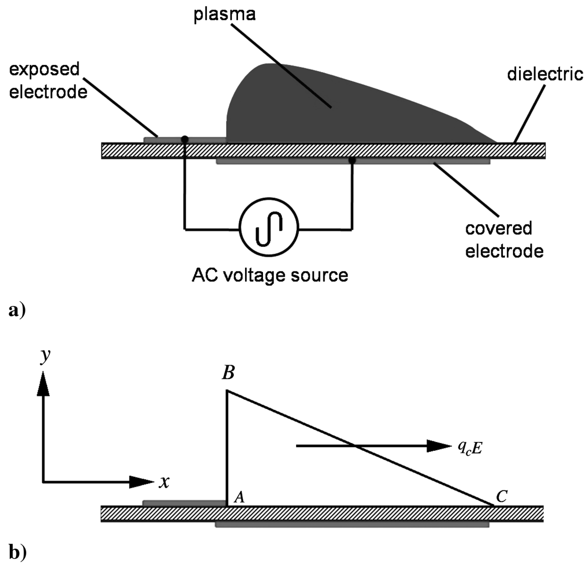

Fig. 1 Plasma actuator: a) schematic representation and b) geometry for the empirical plasma-force model.

The model for the geometric extent of the plasma field generated by such an actuator is indicated in Fig. 1b. The triangular region defined by the line segments AB, AC, and BC constitutes the plasma boundary. Outside of this region, the electric field is not considered strong enough to ionize the air [27]. The electric field has its maximum value at point A and varies linearly within ABC. The peak value of the electric field can be estimated from the applied voltage and the spacing between the electrodes. Along the segment BC, the electric field diminishes to its threshold value, which was taken as 30 kV/cm [27]. The electric body force is equal to $q_c\boldsymbol{E}$ and provides coupling from the plasma to the fluid, resulting in the source vector $\boldsymbol{S}$, appearing in Eq. (1). Some uncertainty exists regarding the direction of the force vector, which was related to the ratio AB/AC in the original work of Shyy et al. [27]. Within the region ABC, the charge density q_c is taken to be constant. The plasma scale parameter D_c arises from nondimensionalization of the governing equations and represents the ratio of the electrical force of the plasma to the inertial force of the fluid.

Some specific details of the plasma model incorporated in the present simulations were specified corresponding to the original experiment of Shyy et al. [27]. The ratio of the threshold electric field magnitude to its peak value was set to 0.133. Referring to Fig. 1b), the distance AC was taken as the length of the covered electrode minus the overlap, and AB varied for different actuator operations (continuous or pulsed). For the purposes of the present computations, it is assumed that actuator was mounted flush with the dielectric surface and did not protrude above it. Because of empiricism of the formulation, there is ambiguity regarding the value of the scale parameter D_c.

A number of other techniques are available for obtaining a plasma-force model and coupling it to the governing equations. The authors [20] described alternate approaches, which we have previously used for a transitional flow control application.

IV. Numerical Method

Time-accurate solutions to Eq. (1) were obtained numerically by the implicit approximately factored finite-difference algorithm of Beam and Warming [28] by employing Newton-like subiterations [29], which have evolved as an efficient tool for generating solutions to a wide variety of complex fluid flow problems and may be written as follows:

$$\begin{aligned}&\left[\frac{1}{\mathcal{J}} + \left(\frac{2\Delta t}{3}\right)\delta_{\xi 2}\left(\frac{\partial \boldsymbol{F}^p}{\partial \boldsymbol{Q}} - \frac{1}{Re}\frac{\partial \boldsymbol{F}_v^p}{\partial \boldsymbol{Q}}\right)\right]\mathcal{J} \times \left[\frac{1}{\mathcal{J}} + \left(\frac{2\Delta t}{3}\right)\delta_{\eta 2}\left(\frac{\partial \boldsymbol{G}^p}{\partial \boldsymbol{Q}}\right.\right.\\ &\quad\left.\left.-\frac{1}{Re}\frac{\partial \boldsymbol{G}_v^p}{\partial \boldsymbol{Q}}\right)\right]\mathcal{J} \times \left[\frac{1}{\mathcal{J}} + \left(\frac{2\Delta t}{3}\right)\delta_{\zeta 2}\left(\frac{\partial \boldsymbol{H}^p}{\partial \boldsymbol{Q}} - \frac{1}{Re}\frac{\partial \boldsymbol{H}_v^p}{\partial \boldsymbol{Q}}\right)\right]\Delta \boldsymbol{Q}\\ &\quad = -\left(\frac{2\Delta t}{3}\right)\left[\left(\frac{1}{2\Delta t}\right)\left(\frac{3\boldsymbol{Q}^p - 4\boldsymbol{Q}^n + \boldsymbol{Q}^{n-1}}{\mathcal{J}}\right)\right.\\ &\quad + \delta_{\xi 6}\left(\boldsymbol{F}^p - \frac{1}{Re}\boldsymbol{F}_v^p\right) + \delta_{\eta 6}\left(\boldsymbol{G}^p - \frac{1}{Re}\boldsymbol{G}_v^p\right)\\ &\quad \left. + \delta_{\zeta 6}\left(\boldsymbol{H}^p - \frac{1}{Re}\boldsymbol{H}_v^p\right) - D_c q_c \boldsymbol{S}^p\right]\end{aligned} \tag{12}$$

In this expression, which is employed to advance the solution in time, $\boldsymbol{Q}^{p+1}$ is the $p+1$ approximation to $\boldsymbol{Q}$ at the $n+1$ time level $\boldsymbol{Q}^{n+1}$, and $\Delta\boldsymbol{Q}=\boldsymbol{Q}^{p+1}-\boldsymbol{Q}^{p}$. For $p=1$, $\boldsymbol{Q}^{p}=\boldsymbol{Q}^{n}$. Second-order-accurate backward-implicit time differencing was used to obtain temporal derivatives.

The implicit segment of the algorithm [left-hand side of Eq. (12)] incorporates second-order-accurate centered differencing for all spatial derivatives and uses nonlinear artificial dissipation [30] to augment stability. Efficiency is enhanced by solving this implicit portion of the factorized equations in diagonalized form [31]. Temporal accuracy, which can be degraded by use of the diagonal form, is maintained by using subiterations within a time step. This technique has been commonly invoked in order to reduce errors due to factorization, linearization, diagonalization, and explicit application of boundary conditions. It is useful for achieving temporal accuracy on overset zonal mesh systems and for a domain decomposition implementation on parallel computing platforms. Any deterioration of the solution caused by use of artificial dissipation and by lower-order spatial resolution of implicit operators is also reduced by the procedure. Three subiterations per time step have been applied in the current simulations to preserve second-order temporal accuracy.

The compact difference scheme employed on the right-hand side of Eq. (12) is based upon the pentadiagonal system of Lele [32] and is capable of attaining spectral-like resolution. This is achieved through the use of a centered implicit difference operator with a compact stencil, thereby reducing the associated discretization error. For the present computations, a sixth-order tridiagonal subset of Lele's system is used, which is illustrated here in one spatial dimension as

$$\alpha\left(\frac{\partial \boldsymbol{F}}{\partial\xi}\right)_{i-1}+\left(\frac{\partial \boldsymbol{F}}{\partial\xi}\right)_{i}+\alpha\left(\frac{\partial \boldsymbol{F}}{\partial\xi}\right)_{i+1}=a\left(\frac{\boldsymbol{F}_{i+1}-\boldsymbol{F}_{i-1}}{2}\right)+b\left(\frac{\boldsymbol{F}_{i+2}-\boldsymbol{F}_{i-2}}{4}\right) \tag{13}$$

with $\alpha=1/3$, $a=14/9$, and $b=1/9$. The scheme has been adapted by Visbal and Gaitonde [33] as an implicit iterative time-marching technique, applicable for unsteady vortical flows, and has been used to obtain the spatial derivative of any scalar, flow variable, metric coefficient, or flux component. It is used in conjunction with a low-pass Padé-type nondispersive spatial filter developed by Gaitonde et al. [34], which has been shown to be superior to the use of explicitly added artificial dissipation for maintaining both stability and accuracy on stretched curvilinear meshes [33]. The filter is applied to the solution vector sequentially in each of the three computational directions following each subiteration, and it is implemented in one dimension as

$$\alpha_f\hat{\boldsymbol{Q}}_{i-1}+\hat{\boldsymbol{Q}}_{i}+\alpha_f\hat{\boldsymbol{Q}}_{i+1}=\sum_{n=0}^{4}\frac{a_n}{2}(\boldsymbol{Q}_{i+n}+\boldsymbol{Q}_{i-n}) \tag{14}$$

where $\hat{\boldsymbol{Q}}$ designates the filtered value of $\boldsymbol{Q}$. It is noted that the filtering operation is a postprocessing technique applied to the evolving solution in order to regularize features that are captured but poorly resolved. Equation (14) represents a one-parameter family of eighth-order filters, for which numerical values for the a_n may be found in [35]. The filter coefficient α_f is a free adjustable parameter that may be selected for specific applications and has been set to 0.30 for the present simulations.

The aforementioned features of the numerical algorithm are embodied in a parallel version of the time-accurate three-dimensional computer code FDL3DI [35], which has proven to be reliable for steady and unsteady fluid flow problems, including vortex breakdown [36,37], transitional wall jets [38], synthetic jet actuators [39], roughness elements [40], plasma flows [16–21], and direct numerical and large-eddy simulations of subsonic [41,42] and supersonic flowfields [43,44].

V. Large-Eddy Simulation Approach

In the LES approach, physical dissipation at the Kolmogorov scale is not represented, thereby allowing for less spatial resolution and a savings in computational resources. For nondissipative numerical schemes, without use of subgrid-scale (SGS) models, this leads to an accumulation of energy at high mesh wave numbers and, ultimately, to numerical instability. Traditionally, explicitly added SGS models are then employed as a means to dissipate this energy. In the present methodology, the effect of the smallest fluid structures is accounted for by an implicit LES (ILES) technique, which has been successfully used for a number of turbulent and transitional computations. The present ILES approach was first introduced by the authors [45] and Visbal et al. [46] as a formal alternative to conventional methodologies and is predicated upon the high-order compact differencing and low-pass spatial filtering schemes, without the inclusion of additional SGS modeling. This technique is similar to monotonically integrated LES (MILES) [47], in that it relies upon the numerical solving procedure to provide the dissipation that is typically supplied by conventional SGS models. Unlike MILES, however, dissipation is contributed by the aforementioned high-order Padé-type low-pass filter at only high spatial wave numbers, for which the solution is poorly resolved. This provides a mechanism for the turbulence energy to be dissipated at scales that cannot be accurately resolved on a given mesh system, in a fashion similar to subgrid modeling. For purely laminar flows, filtering may be required to maintain numerical stability and preclude a transfer of energy to high-frequency spatial modes due to spurious numerical events. The ILES methodology thereby permits a seamless transition from LES to direct numerical simulation as the resolution is increased. In the ILES approach, the unfiltered governing equations may be employed, and the computational expense of evaluating subgrid models, which can be substantial, is avoided. This procedure also enables the unified simulation of flowfields in which laminar, transitional, and turbulent regions simultaneously coexist.

It should also be noted that the ILES technique may be interpreted as an approximate deconvolution SGS model [48], which is based upon a truncated series expansion of the inverse filter operator for the unfiltered flowfield equations. Mathew et al. [49] have shown that filtering provides a mathematically consistent approximation of unresolved terms arising from any type of nonlinearity. Filtering regularizes the solution, and generates virtual subgrid model terms that are equivalent to those of approximate deconvolution.

VI. Isolated Actuator in Ambient Air

A schematic representation of the experimental plasma actuator is shown in Fig. 1. The covered electrode was 0.051 m in length, the exposed electrode was 0.016 m long, and a 0.002 m overlap was employed to ensure a uniform plasma in the streamwise direction. The electrodes consisted of 0.00005-m-thick copper foil, and they were separated by a 0.003175-m-thick Teflon dielectric. For the

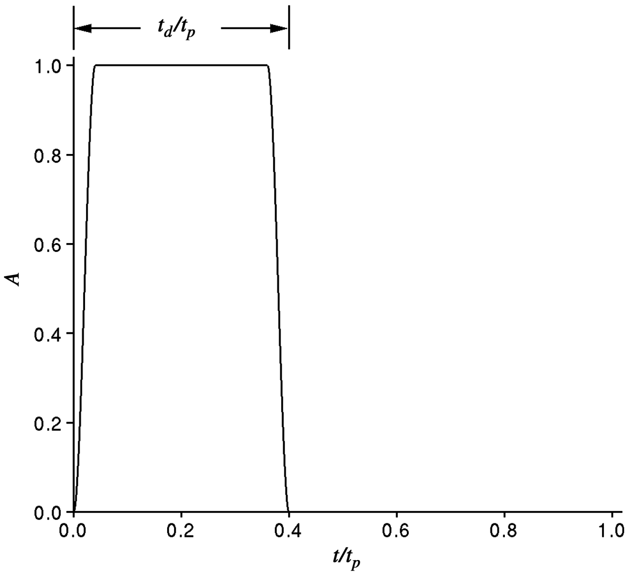

Fig. 2 Pulsing-amplitude-function time history.

Table 1 Plasma-force model parameters

Mode of operation	AB/AC	D_c
Continuous	0.3	4.5
Pulsed	1.0	4.0

purpose of all simulations, the exposed electrode was assumed to lie flat against the dielectric surface. In the experimental arrangement, the transverse extent (z direction) of the actuator covered about 60% of the wind-tunnel span. As the LESs would not account for the tunnel walls or edge effects produced by the finite-span actuator, the plasma force was assumed to be homogeneous in the z direction. Because of this assumption, and the expectation that no fine-scale fluid structures would be generated by the isolated actuator, only two-dimensional simulations were carried out for the ambient situation.

Experimental measurements for the isolated actuator were conducted using a peak-to-peak voltage of 40 kV. For the pulsed case, a 40% duty cycle was employed, which was applied at a frequency of 20 Hz. To numerically represent the duty cycle, a time-dependent amplitude function A was applied as a factor to the electric field arising from the empirical plasma model. The amplitude function is illustrated in Fig. 2, where t_d is the portion of the fundamental period t_p over which the device is active. The ratio $t_d/t_p \times 100$, expressed as a percentage, is the duty cycle, corresponding to 40% in the present case. An amplitude time history for one cycle (appearing in the figure) consists of a series of piecewise cubic and linear functions with continuous derivatives that describe the pulsing. This representation is identical to that used in some previous flow control simulations [19,21,50].

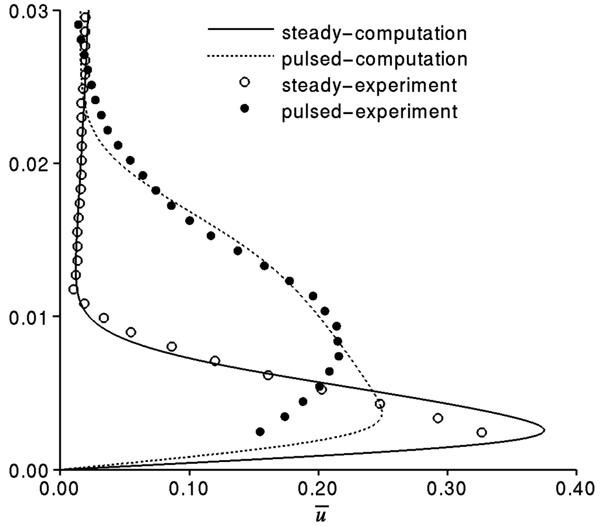

Fig. 3 Time-mean streamwise velocity profiles for isolated actuator in ambient air.

Two-dimensional computations for the isolated actuator were carried out for both continuous and pulsed operations. The streamwise extent of the electric field AC was taken as the length of the covered electrode minus the overlap (0.049 m). Parametric studies were then conducted, during which the ratio AB/AC, the scale parameter D_c, and the vertical y force component were varied. Comparison of the simulated velocity profiles, with measured data at a location downstream of the actuator, was used as a criterion to determine the choice of the parameters that best matched the experiment. It was found that the optimal choice of the force vector had no component in the vertical direction. Other results of the study appear in Table 1. These values then remained fixed for actuators used in subsequent flow control simulations.

It should be noted that the actuator configuration in Fig. 1 is somewhat different than that of the fundamental Shyy et al. [27] model. In particular for that model, the exposed and covered electrodes were of equal lengths in the streamwise direction and did not overlap, so that they were separated by a finite distance. It should further be noted that the plasma scale parameter D_c depends upon the magnitude of the electric field surrounding the actuator, which typically cannot be measured directly and is, therefore, considered a variable parameter in the present simulations.

Found in Fig. 3 is a comparison of the computed results with the data of Schatzman and Thomas [22]. These profiles were taken at a location that was 0.075 m downstream from the origin of the actuator (origin is at the downstream end of the exposed electrode). Although the simulations compare reasonably well with the experiment for the outer portions of the profiles, disparities are evident in the near-wall region. These could be due to inadequacy of the two-dimensional assumption or a basic deficiency in the plasma-force model. No other choices of the model parameters resulted in better agreement.

VII. Flat Plate Without Control

One of the most crucial aspects of this investigation is a LES of the turbulent boundary-layer flow on the flat-plate section upstream of the curved ramp. Conditions in this region must closely match those of the experiment so that a valid comparison of the numerical results can be made with measured data. The simulation of a spatially evolving turbulent boundary is, in itself, a challenging computation. When performing an LES for such flows, the boundary layer

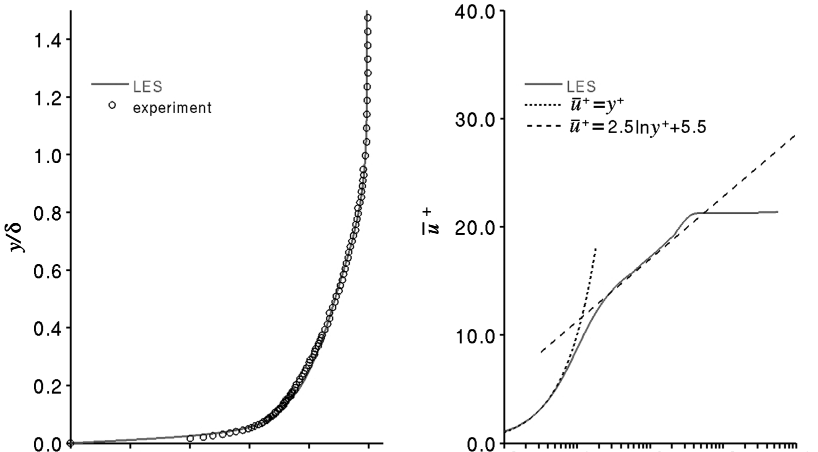

a) b)

Fig. 4 Time-mean streamwise velocity profiles for the flat plate without control: a) in outer variables and b) in law-of-the-wall variables.

Table 2 Computational mesh parameters for the flat plate

Parameter	Value
Grid size	$595 \times 206 \times 205$
Time step	0.0001
Δx^+	29.09
Δy_w^+	0.73
Δz^+	8.94
Δt^+	0.07

typically must be perturbed in order to generate a transition to turbulence.

A. Computational Mesh

The computation mesh for the flat-plate simulation consisted of a nonuniform Cartesian system with a resolved region that extended for 1.0 m in the streamwise x direction. Following this was an additional 4.0 m length to the downstream boundary, where deliberately large grid stretching was implemented. In the vertical direction y, the domain size corresponded to the distance from the plate to the ceiling of the wind tunnel, replicating the configuration of the experiment. The domain size in the spanwise z direction was 0.123 m, which represented 4.63 boundary-layer heights at the x location of the profile shown in Fig. 4. By comparison, in the experiment, the width of the wind tunnel was 0.610 m. The computational mesh consisted of $595 \times 206 \times 205$ grid points in x, y, and z, respectively. The streamwise mesh was clustered near an upstream tripping actuator (to be subsequently discussed) and developed to a uniform spacing that described the final 0.78 m of the plate. The constant mesh size in that region was $\Delta x = 0.002$. Grid spacing in the vertical direction was clustered near the plate surface, where $\Delta y = 0.00005$ and resulted in 105 mesh points lying in the boundary layer and 12 points situated with $y^+ \leq 10$ for the profile in Fig. 4. A uniform distribution of grid points was used in the spanwise direction, where $\Delta z = 0.000615$. Mesh spacings in wall units are given in Table 2, which lie in the range of commonly accepted values for LES [51].

B. Boundary Conditions

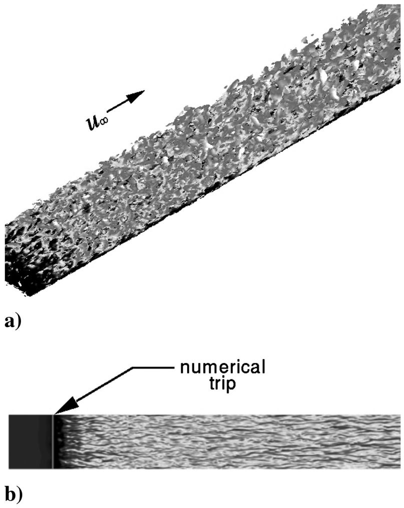

Fig. 6 Instantaneous results for the flat plate without control: a) isosurface of streamwise vorticity and b) contours of streamwise velocity.

At the upstream inflow boundary, all dependent variables were prescribed from a two-dimensional computation, except for the pressure, which was extrapolated from the interior solution to preclude the formation of trapped waves. Along the downstream outflow boundary, the exit static pressure was fixed at the freestream value p_∞, and other flow variables were extrapolated from within the

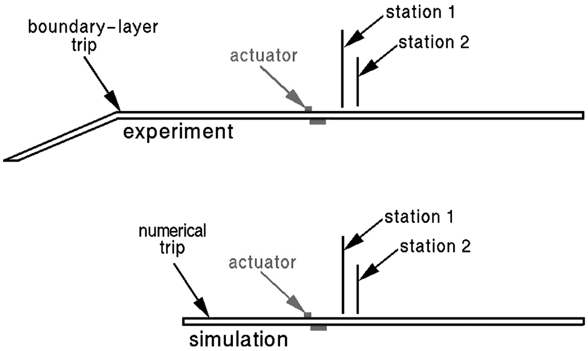

Fig. 7 Schematic representation of the boundary-layer developmental plate configuration.

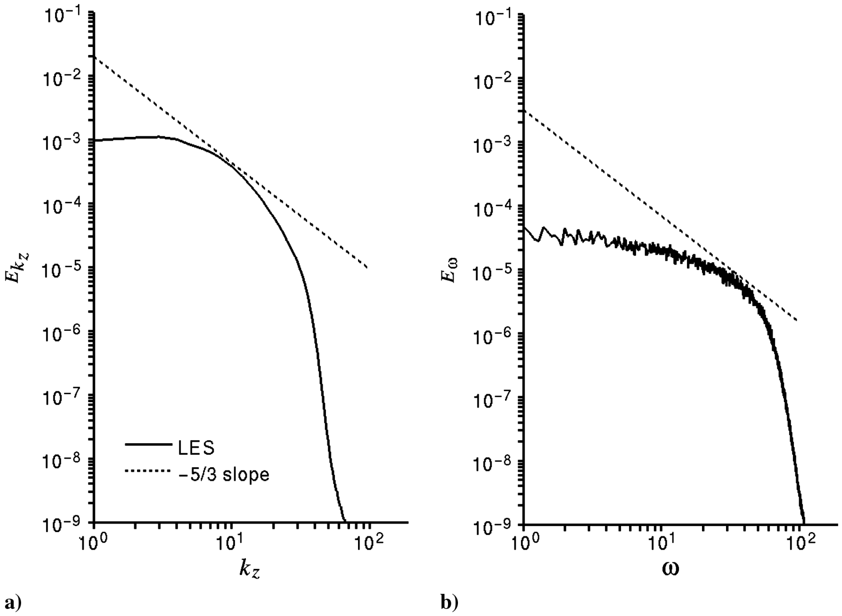

Fig. 5 Turbulent-kinetic-energy spectra for the flat plate without control: a) time-mean spanwise wave number and b) spanwise-averaged frequency.

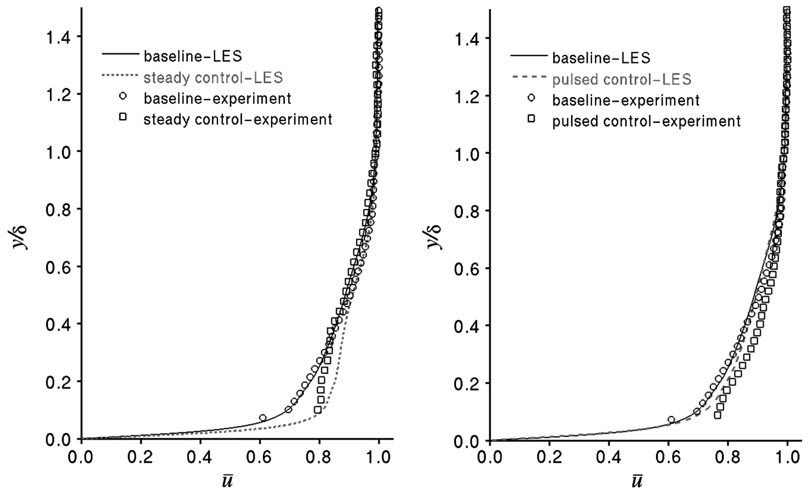

a) b)

Fig. 8 Time-mean streamwise velocity profiles at station 1 for the flat plate with control: a) continuous actuation and b) pulsed actuation.

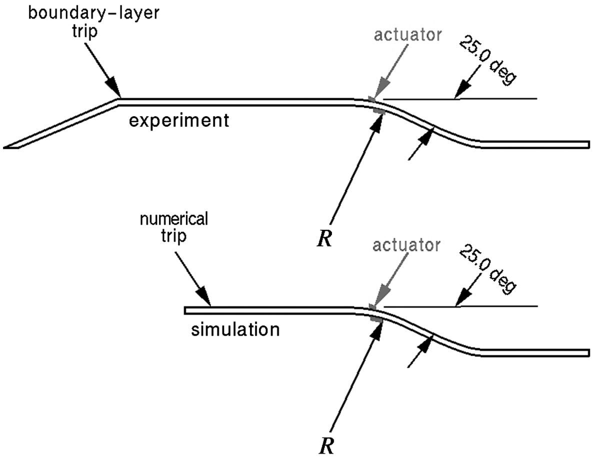

Fig. 9 Schematic representation of the plate/ramp combination configuration.

interior domain. Streamwise grid stretching in the outflow region prevented spurious reflections from the outflow boundary. This technique transfers information to high spatial wave numbers and then dissipates it by the low-pass numerical filter [52]. On the plate surface, the no-slip condition was enforced, along with an isothermal wall and a third-order-accurate implementation of a zero normal pressure gradient. Inviscid slipped-wall conditions were applied at the upper vertical boundary, corresponding to the wind-tunnel ceiling. Periodic conditions were invoked for the spanwise direction by applying a five-plane overlap of grid points at the z boundaries.

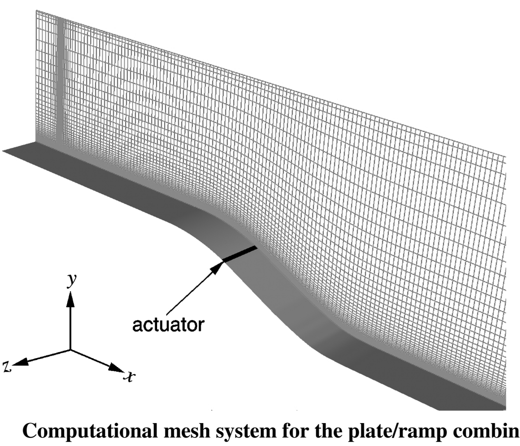

Fig. 10 Computational mesh system for the plate/ramp combination.

C. Temporal Considerations

Computations were performed with a time step of $\Delta t = 0.0001$. As noted in Table 2, this satisfied the criteria $\Delta t^+ = \mathcal{O}(1)$, which represents the viscous time scale in the wall sublayer [53]. Statistical information collected to obtain the time-mean flow used 100,000 time steps corresponding to 10.0 characteristic units. For the ensuing pulsed control simulations, the duty cycle was constructed by 2500 time steps, such that the statistical collection period consisted of 40 periods of actuation.

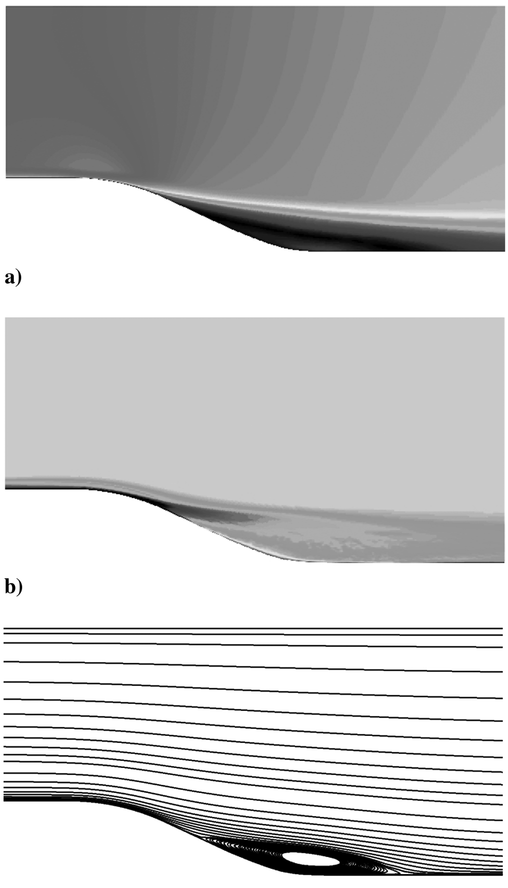

a)

b)

c)

Fig. 11 Time-mean results for the baseline plate/ramp combination: a) velocity magnitude q contours, b) spanwise vorticity contours, and c) streamlines.

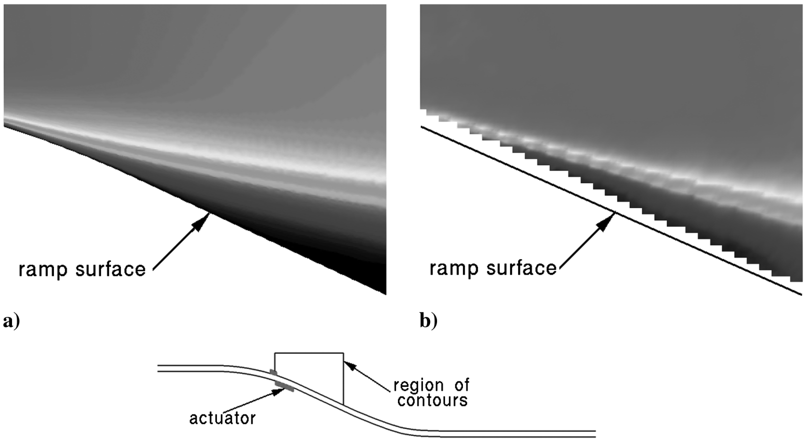

Fig. 12 Time-mean velocity magnitude q contours for the baseline plate/ramp combination: a) LES and b) experiment.

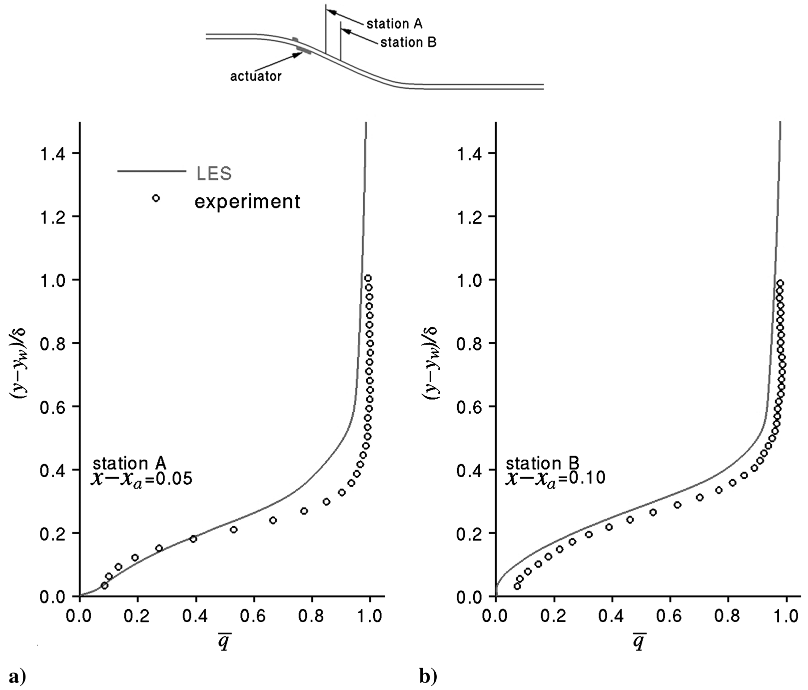

Fig. 13 Time-mean velocity magnitude q profiles for the baseline plate/ramp combination: comparison with experiment.

D. Parallel Processing

For parallel processing, the computational domain was decomposed into a series of subzones, which were then distributed on individual processors of a massively parallel computing platform. The decomposition was constructed to provide an approximately equal number of grid points in every subzone, thereby balancing the computational work load among the processors. Faces at the boundaries of each subzone were overset into adjacent domains, so that an overlap of five planes was established. Although this incurred an overhead due to redundant computation, it maintained the formal high-order accuracy of both the numerical differencing and the filtering schemes. Automated software [54] was used to identify donor and recipient grid points in the overlapping domains. Internode communication among the processors was established through standard message-passing interface library routines [55], which were used to transfer information between the various subzones of the flowfield at domain boundaries. A total of 300 processors was employed for all the plate computations.

E. Results

A preliminary two-dimensional plate calculation was carried out in order to examine computational mesh spacings. Values of dependent variables from that simulation were then specified at the inflow for the fully three-dimensional case. A body force, similar to that of the empirical plasma model, was used as a tripping mechanism to produce a turbulent flow. For this purpose, the force component was directed counter to that of the flow direction ($-x$). This orientation produced a small region of reversed flow, creating an unstable velocity profile that rapidly transitioned to a turbulent state.

Table 3 Computational mesh parameters for the plate/ramp configuration

Grid designation	Grid size	Time step	Δx^+	Δy_w^+	Δz^+	Δt^+
Grid 1	905 × 216 × 205	0.00010	32.07	0.82	10.06	0.09
Grid 1	905 × 216 × 205	0.00005	32.62	0.82	10.03	0.04
Grid 2	790 × 189 × 179	0.00010	37.42	0.90	11.48	0.09
Grid 3	678 × 162 × 154	0.00010	43.86	1.04	13.45	0.09

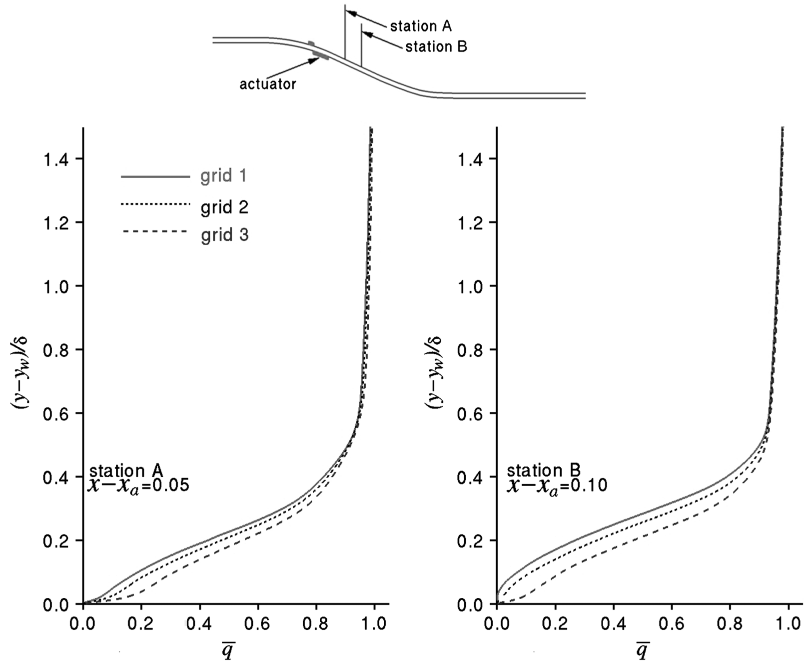

Fig. 14 Time-mean velocity magnitude *q* profiles for the baseline plate/ramp combination: grid sensitivity.

The actuator was located 0.1 m downstream from the inflow boundary and extended 0.005 m in the streamwise direction. The value of the plasma scale parameter D_c was adjusted until it was sufficiently large to just produce transition. The body force was restricted to a very small region, much smaller than that used for the previously described control actuators, with $D_c = 40.0$. The approach for using a plasmalike body force as a tripping mechanism is identical to the previous work of Visbal and Gaitonde [18].

The reference Reynolds number for the LES was $Re = 310,000$, corresponding to that of the experiment, and the Mach number $M_\infty = 0.1$. In the experiment, $M_\infty = 0.015$, but the compressibility effects were not expected to be significant for the computation. After the simulated boundary layer evolved to an equilibrium state, statistical information was collected, and the time-mean flowfield was generated. From the time-mean flow, boundary-layer properties were computed, and the LES was compared with the experiment at a location within the computational domain where the boundary-layer thickness matched that of the experiment. A comparison of the streamwise velocity profiles is presented in Fig. 4a, which indicates good agreement of the LES with the experiment. Provided in Fig. 4b is the same profile, plotted in law-of-the-wall units, which is seen to compare well with the universal logarithmic profile.

The turbulent-kinetic-energy spanwise wave number and frequency spectra are seen in Fig. 5. These spectra were collected at a streamwise location slightly downstream of that for the profiles in Fig. 4 and at a vertical position approximately equal to one-half of the boundary-layer thickness. The wave-number spectra exhibit spatial resolution well beyond the inertial range before the grid cutoff. No amplification of a particular discrete frequency, which might be associated with the numerical tripping mechanism, is observed in Fig. 5b. The spectra display broadband frequency content that is representative of high-Reynolds-number flows.

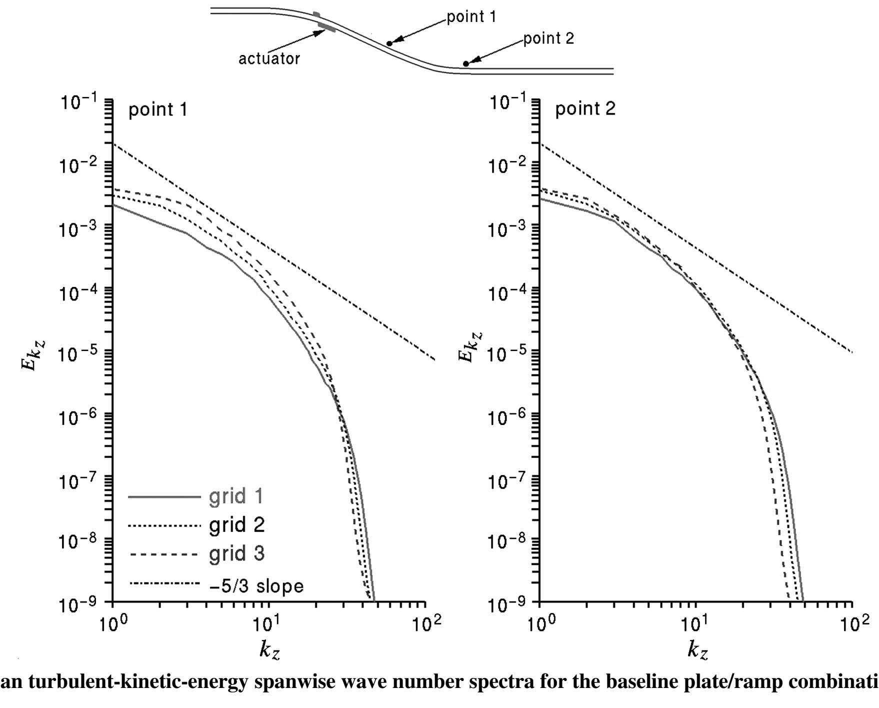

Fig. 15 Time-mean turbulent-kinetic-energy spanwise wave number spectra for the baseline plate/ramp combination: grid sensitivity.

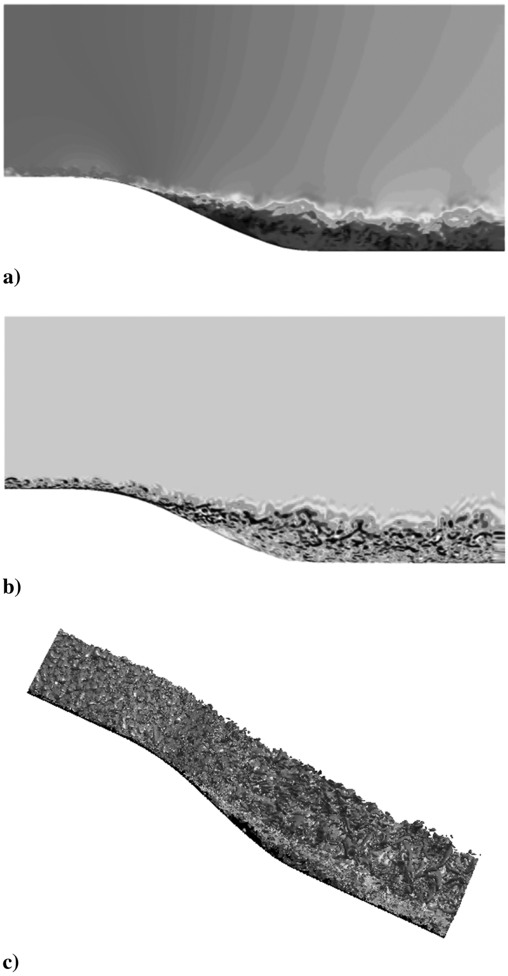

Fig. 16 Instantaneous results for the baseline plate/ramp combination: a) velocity magnitude *q* contours, b) spanwise vorticity contours, and c) isosurface of vorticity magnitude.

Figure 6 displays characteristic features of the instantaneous plate flowfield. An isosurface of the streamwise component of vorticity, colored by the u velocity, in Fig. 6a demonstrates fine-scale fluid structures which are captured in the solution. In Fig. 6b, contours of the streamwise velocity u are shown at a constant vertical location where $y^+ = 9.17$, illustrating the low-speed streaks which are common to turbulent wall-bounded flows.

VIII. Flat Plate with Plasma Control

The experimental configuration for the boundary-layer developmental plate is depicted schematically in Fig. 7. A curved contour brought the flow from the wind-tunnel floor to the leading edge of the plate. Note that the upstream geometry is not portrayed accurately in the figure. A trip strip of sand grain roughness was located at the leading edge of the plate in order to generate transition. The plasma actuator was positioned with the downstream edge of the exposed electrode a distance of 0.762 m from the boundary-layer trip. The actuator was centered across the span of the tunnel, with the covered and exposed electrodes 0.356 and 0.381 m wide, respectively. The two stations appearing in the figure represent streamwise locations at which experimental measurements were taken. Station 1 was 0.837 m from the trip, whereas station 2 was at 0.889 m. Station 2 is the location where boundary-layer profiles from the experiment and computation were compared in Fig. 4. In simulations with plasma flow control, the actuator was positioned relative to station 2 so that it would correspond to that of the experiment.

LESs of the plate boundary layer were carried out for both continuous and pulsed operations of the plasma actuator. Parameters for the force model in these computations were identical to those of Table 1 for the isolated actuator case. The LESs for the control cases were performed in a fashion similar to that of the baseline plate case, and statistical information was collected in the same manner. Profiles of the time-mean streamwise velocity at station 1 are compared with experimental data in Fig. 8. For steady actuation, the LES indicates slightly more control than that of the experiment. With pulsed control, the situation is just the opposite. These disparities may be due to previously noted deficiencies in the plasma-force model for the isolated actuator cases or due to the limited extent of the spanwise domain in the simulations, which make such computations tractable.

IX. Plate/Ramp Combination Without Control

In the experimental configuration, the start of a convex rearward-facing ramp was located 0.914 m downstream of the boundary-layer trip on the developmental plate. The ramp turned through a constant radius arc R of 0.510 m to a maximum deflection of 25.0 deg. Following a straight ramp section, the geometry was curved back to a horizontal orientation. A schematic representation of the configura-

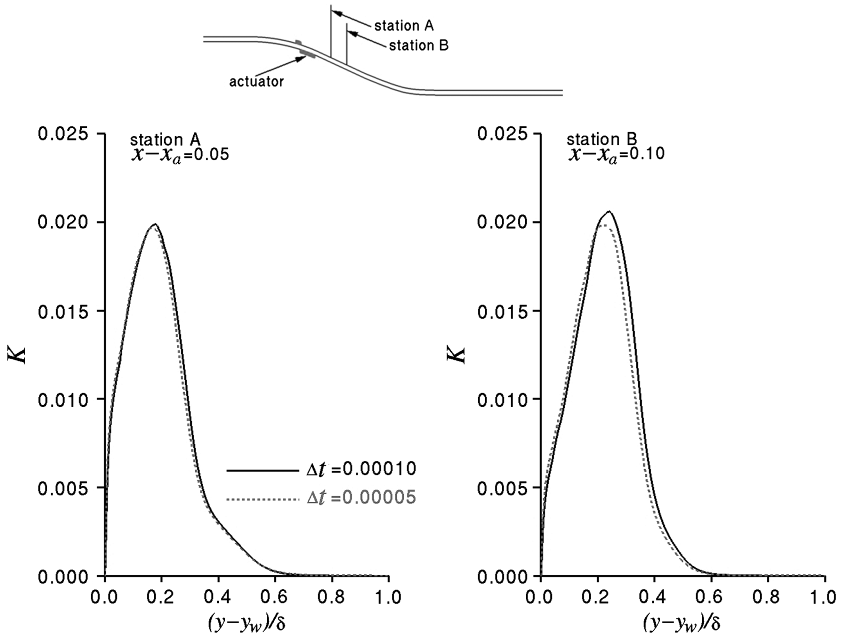

Fig. 17 Time-mean turbulent-kinetic-energy profiles for the baseline plate/ramp combination: effect of time step.

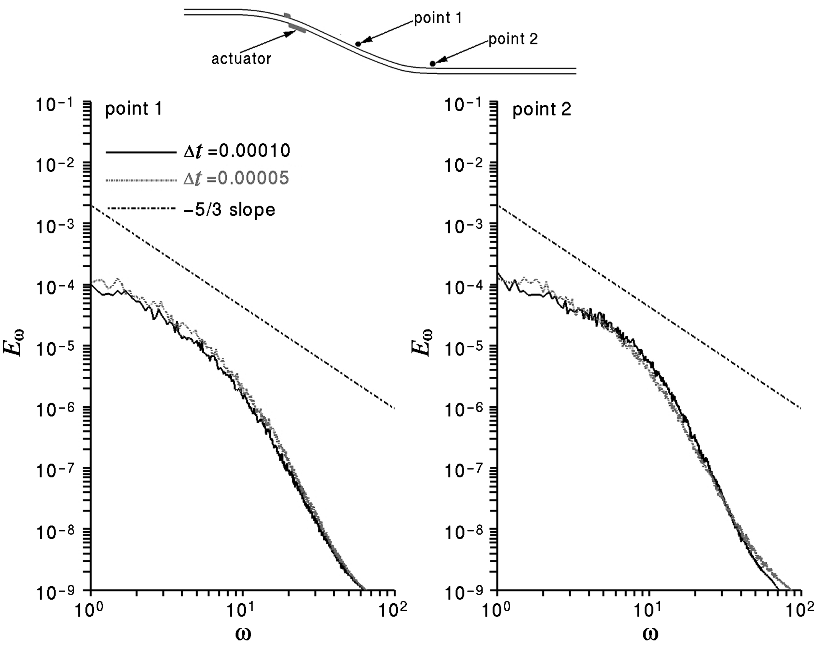

Fig. 18 Spanwise-averaged turbulent-kinetic-energy frequency spectra for the baseline plate/ramp combination: effect of time step.

tion is found in Fig. 9. For the simulations, the streamwise position of the ramp was again located relative to station 2 in Fig. 7, as was done in the plate computations. The plasma actuator was situated where the local ramp angle was 18.0 deg, which was just upstream of the separation point in the experiment.

A computational mesh for the plate/ramp configuration was generated, similar to that of the flat plate. The normal near-wall spacing and spanwise extent of the domain were identical to that used for the plate computation. A constant spacing in the streamwise direction was employed, as previously described, along the plate portion of the configuration and continued for the curved ramp surface downstream of the reattachment point of the separated flow. Eventually, the mesh was stretched to the downstream outflow boundary, which was located 4.95 m downstream from the start of the ramp. The grid consisted of 905 × 216 × 205 points in x, y, and z, respectively, and may be seen in Fig. 10, in which only a fraction of the grid lines are shown. Clustering of mesh points at the tripping location near the inflow boundary can be observed in the figure. Parallel computing was carried out in a fashion similar to that previously described for the flat plate, for which the plate/ramp grid system was distributed over 500 processors.

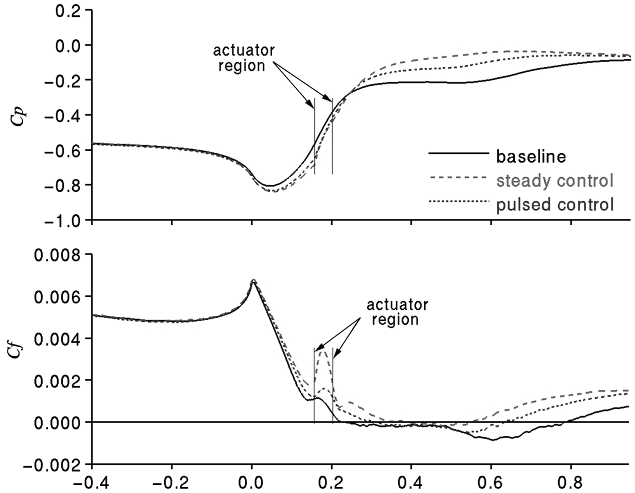

Fig. 19 Time-mean surface pressure and skin-friction coefficient distributions for the plate/ramp combination.

A. Time-Mean Flowfield

The flowfield for the plate/ramp combination was initialized from the flat-plate solution and allowed to temporally evolve for 100,000 time steps in order to attain an equilibrium state. Similar to the plate solution, statistical information was then collected for an additional 100,000 time steps (10 characteristic units). Results of the time-mean

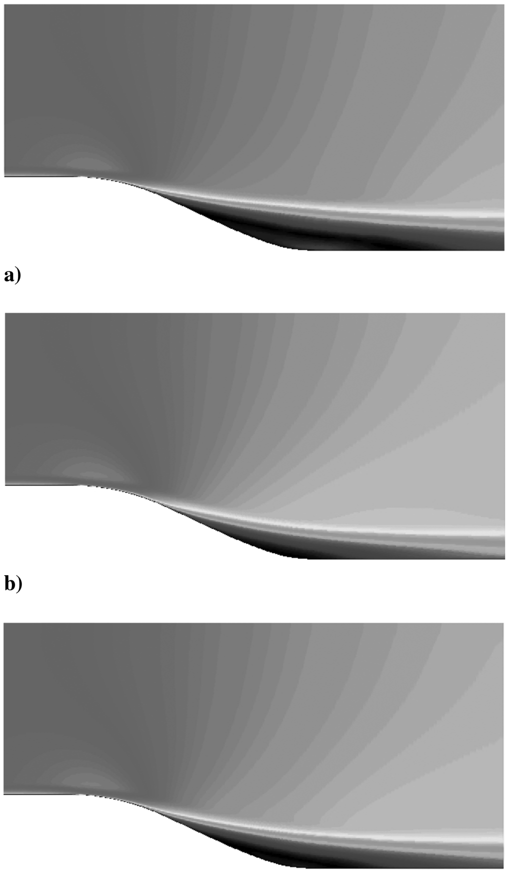

Fig. 20 Time-mean velocity magnitude q contours for the plate/ramp combination: a) baseline, b) continuous actuation, and c) pulsed actuation.

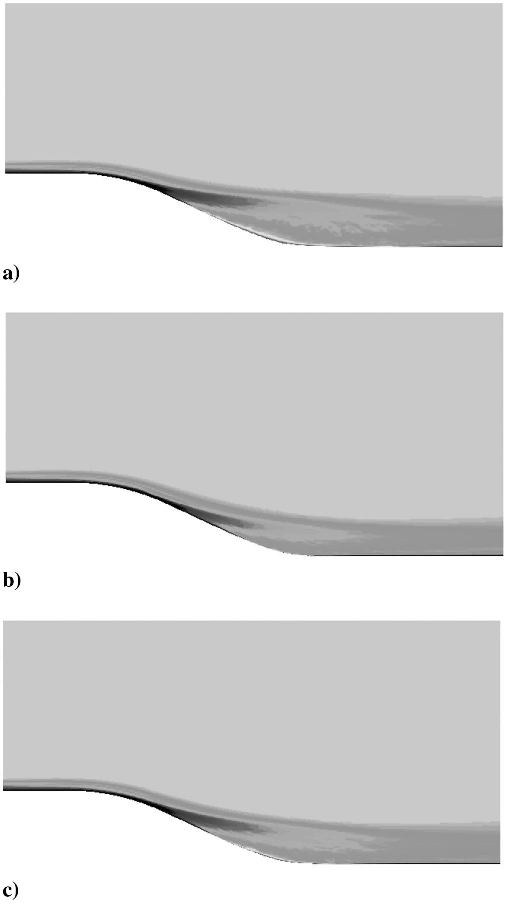

Fig. 21 Time-mean spanwise vorticity contours for the plate/ramp combination: a) baseline, b) continuous actuation, and c) pulsed actuation.

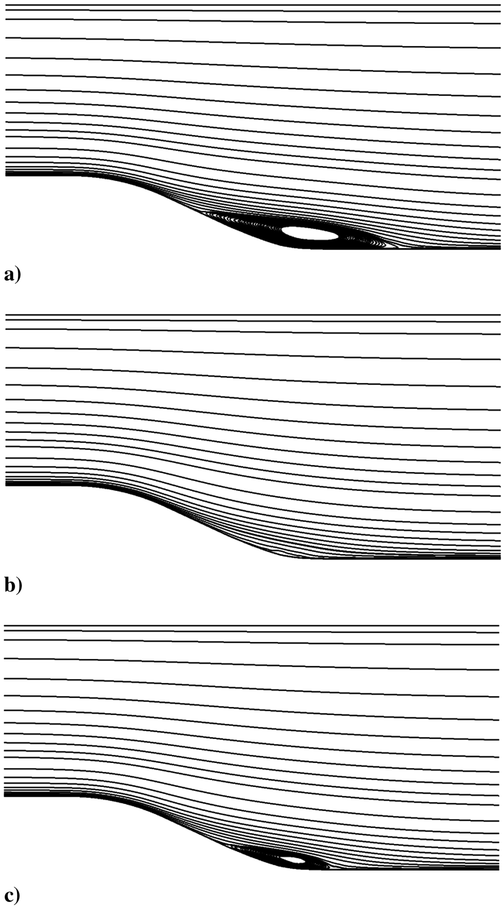

Fig. 22 Time-mean streamlines for the plate/ramp combination: a) baseline, b) continuous actuation, and c) pulsed actuation.

flowfield from this computation are presented in Fig. 11. Figure 11a displays contours of the velocity magnitude, Fig. 11b provides the spanwise vorticity component, and Fig. 11c exhibits the streamline pattern. The significant recirculation region is clearly evident in Fig. 11c. Figure 12 compares velocity magnitude contours from the LES with measurements of the Schatzman and Thomas [22] experiment and demonstrates good agreement. The experimental data were obtained via two-component particle image velocimetry (PIV), details of which may be found in [22]. A more quantitative comparison is given in Fig. 13 by vertical profiles of velocity magnitude. These profiles were extracted directly from the PIV. The two stations at which the comparisons are made were taken at distances of 0.05 and 0.10 m downstream from the trailing edge of the actuator location. These results confirm that the baseline case for flow about the plate/ramp configuration has been reasonably well simulated by the computation.

B. Effect of Spatial Resolution

In addition to the previously described computational mesh system, two supplementary coarser grids were generated in order to investigate the effect of spatial resolution. These grids were constructed such that spacing ratios in all of the nonuniform grid regions were identical to those of the original mesh. Solutions for the baseline flow were obtained on both grids in the same manner as was employed for the more refined simulation. Resulting mesh spacings in wall units from these calculations appear in Table 3. The streamwise location used as the reference state for these spacings is on the upstream flat-plate region, at the same distance from the tripping actuator for which the spacings for the flat plate are reported in Table 2. It can be noted that spacings for the plate/ramp combination (Table 3) are slightly larger than those for flat plate alone (Table 2). This is due to acceleration of the flow over the downstream ramp, which increases the wall shear used in the law-of-the-wall variables.

Figure 14 indicates time-mean velocity magnitude profiles obtained on the three grid systems at the same streamwise locations as was shown in Fig. 13. In all situations, the spacings lie in the range commonly classified as LES. Although the solution on grid 3 is too coarse to correctly capture the separated flow region, a consistent trend with mesh refinement is observed. Although it is well known that there exists no concept of grid independence for LES in the absence of explicit filtering [56], there is an indication of adequate resolution for the solution on grid 1 (original grid).

Further results of the grid resolution study are presented in Fig. 15, which displays time-mean turbulent-kinetic-energy spanwise wave number spectra at two points within the separated flow region. These points lie at distances downstream of the actuator, where $x - x_a = 0.2$ (point 1) and $x - x_a = 0.4$ (point 2), respectively. In both cases, the points are situated a distance from the ramp surface that is equal to one-half of the boundary-layer thickness for attached flow upstream of the ramp. The spectra evidence that resolution in the homogeneous direction z appears to be sufficient.

It should be mentioned that the baseline flow was selected for resolution studies, as its simulation is more demanding than that of the control cases. When plasma actuation is applied, the amount of separation is decreased, leading to a reduction in the overall complexity of the flowfield.

C. Instantaneous Flowfield

Features of the instantaneous flowfield are illustrated in Fig. 16. Velocity magnitude contours are given in Fig. 16a, whereas contours of the spanwise vorticity are depicted in Fig. 16b. These contours were extracted at the midspan location of the computational

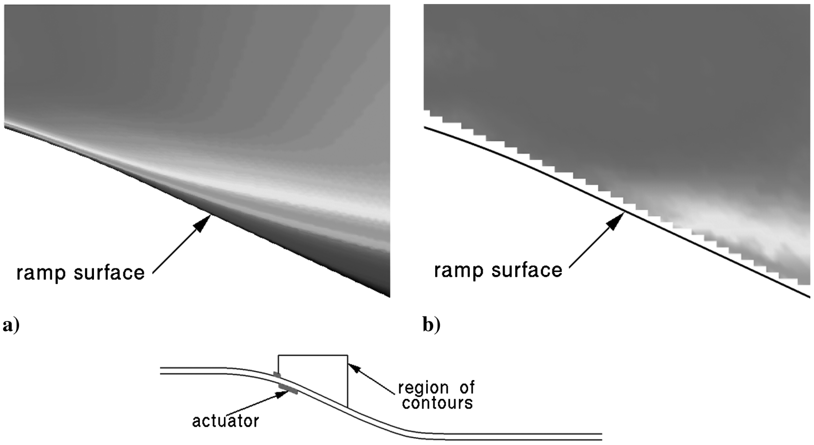

Fig. 23 Time-mean velocity magnitude q contours for continuous actuation of the plate/ramp combination: a) LES and b) experiment.

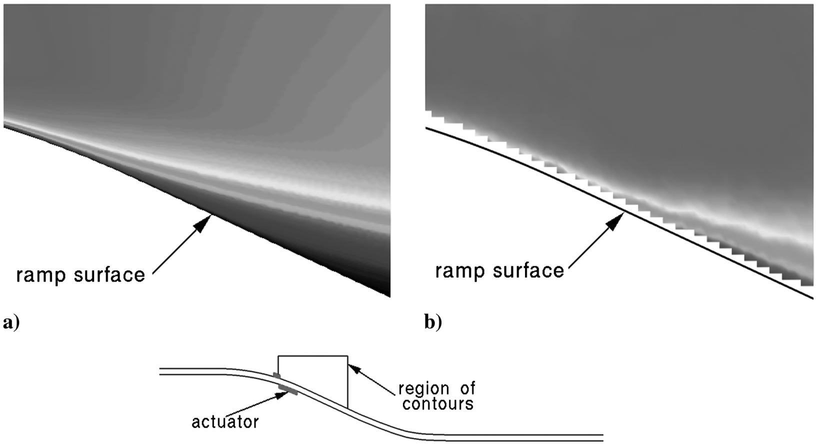

Fig. 24 Time-mean velocity magnitude q contours for pulsed actuation of the plate/ramp combination: a) LES and b) experiment.

flowfield. Massive separation is evident in the cove region, and fine-scale turbulent structures can be seen in Fig. 16b. Figure 16c provides a three-dimensional representation of the instantaneous flowfield, in terms of an isosurface of vorticity magnitude, which has been colored by the streamwise velocity. The value of the isosurface corresponds to that in the outer portion of the boundary layer. Turbulent structures and the separated region are again apparent in the figure.

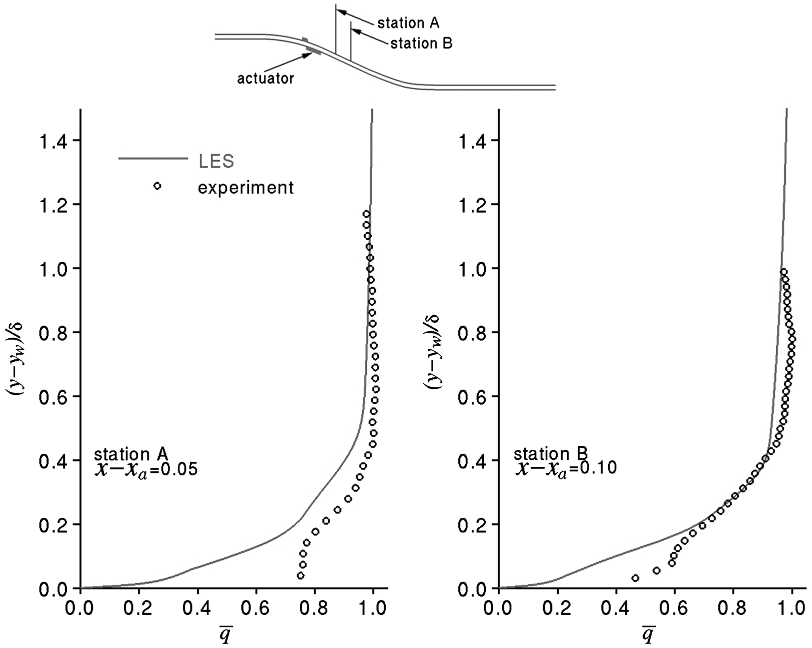

Fig. 25 Time-mean velocity magnitude q profiles for continuous actuation of the plate/ramp combination: comparison with experiment.

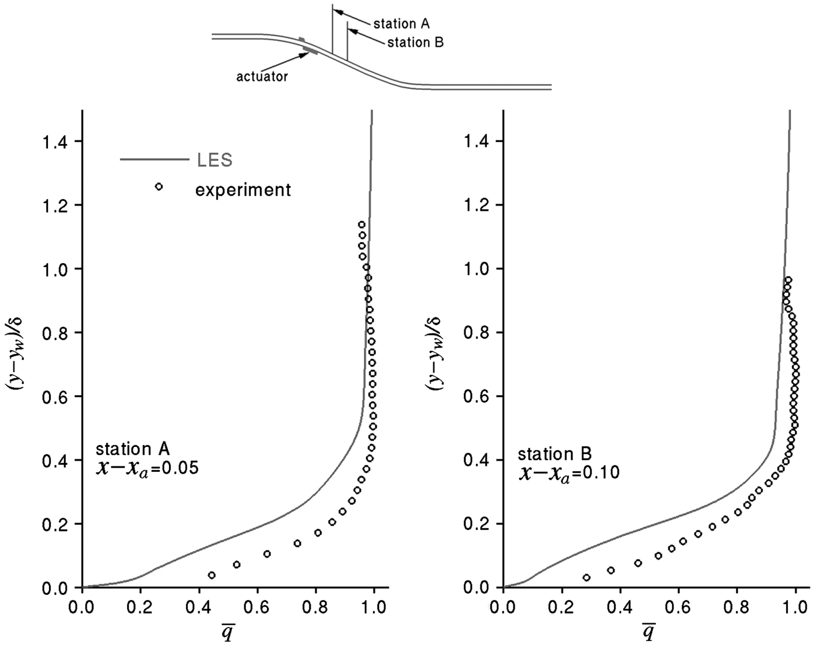

Fig. 26 Time-mean velocity magnitude *q* profiles for pulsed actuation of the plate/ramp combination: comparison with experiment.

D. Effect of Temporal Resolution

To assess the temporal accuracy of the plate/ramp simulation, a solution was generated with a time step that was one-half of the nominal value ($\Delta t = 0.00005$). For this computation, statistical data were accumulated for 200,000 time steps, so that the collection period was identical to that of the previous calculations. Resultant information for the computation may be found in Table 3. Profiles of the time-mean turbulent kinetic energy, obtained using the two different time-step sizes, are compared in Fig. 17. The stations from which these profiles were extracted are the same as those of Figs. 13 and 14. Only minor differences are seen between the two results, which demonstrates that the temporal resolution using the larger time step is sufficient to correctly represent the unsteady turbulent features of the flow.

Additional evidence of the temporal accuracy is indicated by the turbulent-kinetic-energy frequency spectra appearing in Fig. 18. These spectra were obtained at the same locations as those in Fig. 15. Because these points lie deep within the separated flow region, the nature of the spectra is somewhat different than that exhibited within the boundary layer for the flat plate (see Fig. 5). Once again, minimal differences between spectra obtained with two different time steps confirm adequacy of the temporal resolution.

X. Plate/Ramp Combination with Plasma Control

Solutions for the plate/ramp configuration with plasma-based flow control were obtained in a manner similar to that previously described. Both continuous and pulsed actuation were simulated, using the same choice of plasma-force parameters as those obtained for the isolated actuator in ambient air (see Table 1).

A. Time-Mean Flowfields

Time-mean spanwise-averaged surface pressure and skin-friction coefficient distributions are shown in Fig. 19. The control results are compared with each other and with the baseline solution. The origin of the x axis is referenced to the beginning of the curved ramp location x_r. A significant plateau in the surface pressure for the baseline case ($0.3 \leq x - x_r \leq 0.5$) is representative of separated flow. The plateau is diminished for pulsed control and eliminated for steady actuation. The extensive separated flow region for the baseline case is observed in the corresponding skin-friction distributions. With steady control, separation has essentially been removed. For pulsed actuation, although separation has not been eliminated, the extent of the reversed flow region has been greatly reduced.

Time-mean velocity magnitude contours are presented in Fig. 20, which also illustrates the reduction in separation when control is applied. Momentum added to the flow by the actuator helps keep the boundary layer in proximity to the solid surface, as is evident in the spanwise vorticity contours provided in Fig. 21. Reduction of

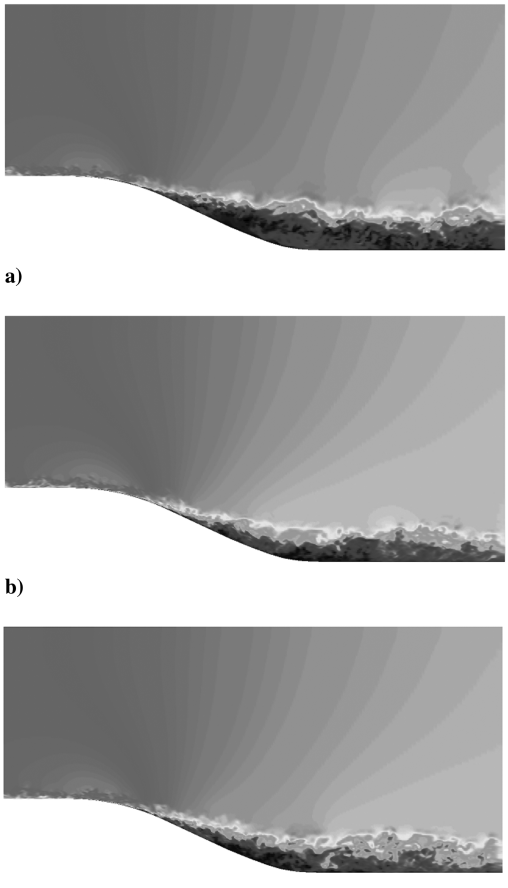

Fig. 27 Instantaneous velocity magnitude *q* contours for the plate/ramp combination: a) baseline, b) continuous actuation, and c) pulsed actuation.

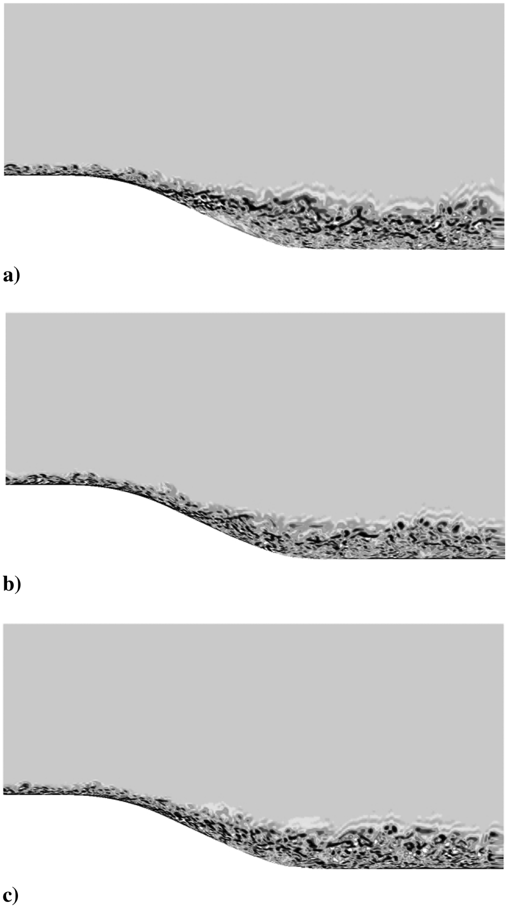

Fig. 28 Instantaneous spanwise vorticity contours for the plate/ramp combination: a) baseline, b) continuous actuation, and c) pulsed actuation.

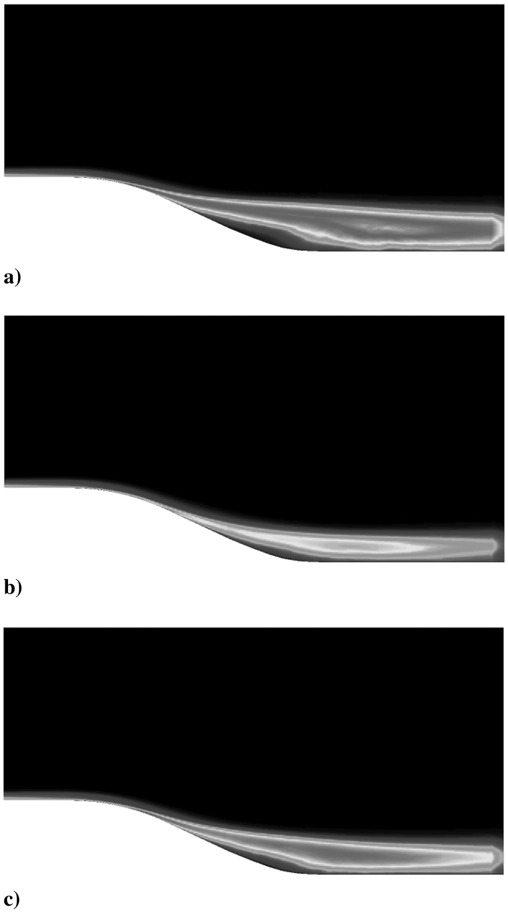

Fig. 30 Time-mean turbulent-kinetic-energy contours for the plate/ramp combination: a) baseline, b) continuous actuation, and c) pulsed actuation.

the recirculating flow region is again apparent in the streamlines depicted in Fig. 22.

Time-mean velocity magnitude contours for the control cases are compared with the experimental PIV in Figs. 23 and 24 for continuous and pulsed actuation, respectively. Although the comparison is generally favorable, there appears to be more control exerted in the experiment than is evident in the simulations. This behavior is also apparent in the velocity magnitude profiles found in Figs. 25 and 26. As in the baseline case, these profiles were extracted from the PIV. Reasonable agreement between the simulation and the experiment in

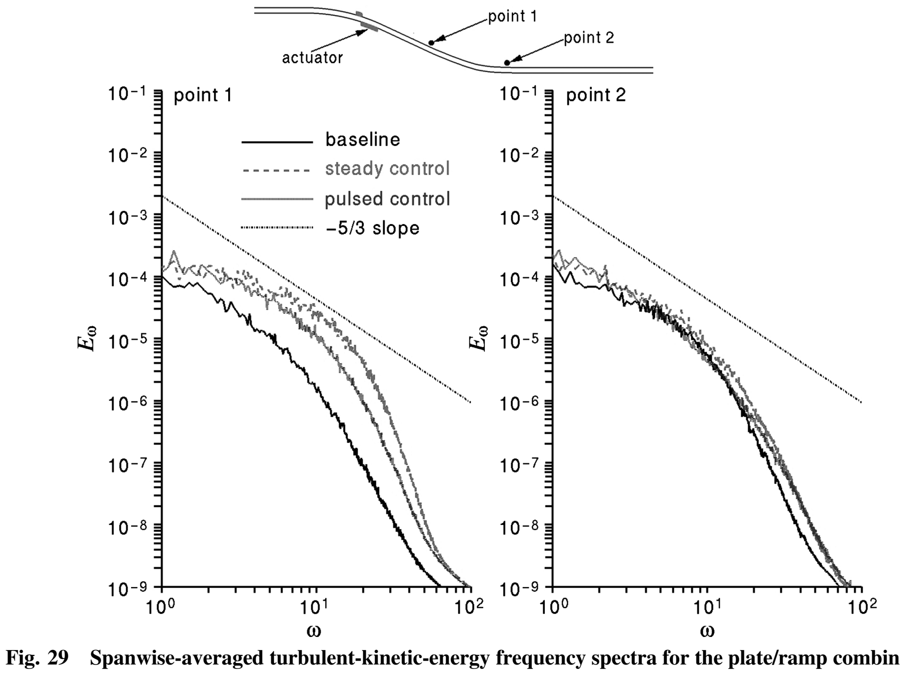

Fig. 29 Spanwise-averaged turbulent-kinetic-energy frequency spectra for the plate/ramp combination.

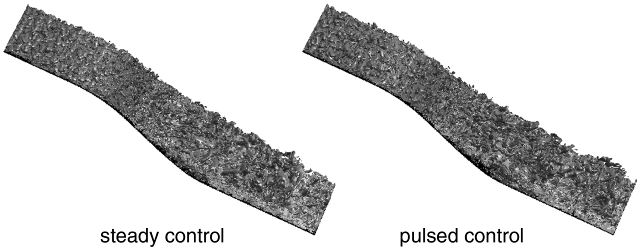

Fig. 31 Instantaneous isosurface of vorticity magnitude for the plate/ramp combination.

the outer portion of the boundary layer for continuous actuation is seen in Fig. 25. A similar comparison is evident with pulsed control in Fig. 26. The major disparities in both cases occur in the near-wall region and are likely due to deficiencies associated with the plasma-force model. These were also noted for the isolated actuator in ambient air.

B. Instantaneous Flowfields

Instantaneous flowfields of the control cases are represented by the velocity magnitude and the spanwise vorticity contours in Figs. 27 and 28, respectively. Here, again, a decrease in the vertical extent of the separated boundary layer is indicated when flow control is applied. Turbulent-kinetic-energy spanwise wave number spectra are shown in Fig. 29. The spectra are similar to those of the baseline case, but the magnitudes are higher due to energy addition by plasma actuation. This is particularly noticeable at point 1. The pulsing actuation frequency $\omega = 4.0$ does not seem to produce a local peak in the spectra, because points 1 and 2 are somewhat far downstream from the actuator and are embedded in the separated flow region.

Provided in Fig. 30 are time-mean contours of the turbulent kinetic energy. Even though energy has been supplied locally to the flow via plasma actuation, the contours indicate an overall reduction in the turbulent kinetic energy when control is applied. This is consistent with a decrease in the amount of separation and a reduction in turbulent complexity for the actuated situations. Isosurfaces of vorticity magnitude for the control cases are presented in Fig. 31. These are quite similar to the baseline case. Because the value of the isosurface corresponds to that of the outer portion of the boundary layer, the reduction in the separated flow region is not readily apparent in this illustration.

XI. Conclusions

A comprehensive set of numerical computations was performed in order to validate use of an empirical model for the simulation of plasma-based flow control. This model was used to represent the electric field about a plasma actuator, thus providing a body force acting upon the surrounding fluid and making it possible to perform LESs of complex turbulent flowfields. The calculations included those for an isolated actuator in ambient air, which were used to optimize several of the parameters inherent in the empirical model, as well as control situations for the turbulent boundary on a flat plate and the case of massively separated flow over a curved convex rearward-facing ramp configuration.

All simulations were carried out with a high-order numerical method. The baseline case for a flat plate without control was found to agree well with experimental data and with the universal logarithmic profile, indicating that the fully turbulent flow had been simulated correctly. Spatial grid resolution and time-step studies for the plate/ramp configuration confirmed accuracy of the complex separated flow situation.

Simulations with plasma-based control were conducted with both continuous and pulsed actuation. Although the overall comparison between the computations and the experimental measurements was generally favorable, deficiencies were observed in the near-wall flow region. This was true for the isolated actuator, as well as for the plate/ramp combination. It should be noted that the arrangement of electrodes in the present actuator was somewhat different from those of the original empirical model [27], which probably contributed to the observed differences between the computations and the experiments.

Although the empirical model has previously been employed for the numerical study of plasma-based flow control [16–21], in the past, there were no experimental data available for comparison at the same flow conditions of the simulations. The present investigation allows for that comparison. In addition, many of the previous studies considered flows at lower Reynolds numbers that were transitional or not fully turbulent. The computations considered in the current work allow for an assessment of LES, used in conjunction with the empirical model, for application of plasma-based control to fully turbulent wall-bounded flows that are characteristic of high-Reynolds-number situations.

Values of the plasma scale parameter D_c used in these simulations are somewhat smaller than those specified in prior computations [16–21]. This is because the extent of the actuator in the streamwise direction is larger than that of previous simulations, so that the power requirements are similar. Specification of D_c requires knowledge of the electric field magnitude surrounding the actuator, which is generally unknown and difficult to measure. As a result, D_c can only be estimated. Although not calculated directly, the availability of experimental data for the flowfield surrounding the actuator has allowed parametric variation of D_c to best match the measurements. This is something that has not previously been possible. Although certain shortcomings of the model have been identified, it has been shown to be adequate for predicting the dominant effects of plasma actuators, thus permitting its use for investigating plasma-based flow control strategies through LES.

Acknowledgments

The work presented here was sponsored by the U.S. Air Force Office of Scientific Research. Computational resources were supported in part by a grant of supercomputer time from the U. S. Department of Defense Major Shared Resource Center, Wright-Patterson Air Force Base, OH. The authors are grateful to D. M. Schatzman and F. O. Thomas for supplying details of their investigations and the associated experimental data, and they also wish to acknowledge P. E. Morgan for helpful conversations.

References

[1] Lorber, P., McCormick, D., Anderson, T., Wake, D., MacMartin, D., Pollack, M., Corke, T., and Breuer, K., “Rotorcraft Retreating Blade Stall Control,” AIAA Paper 2000-2475, June 2000.

[2] Corke, T. C., Jumper, E. J., Post, M. L., Orlov, D., and McLaughlin, T. E., “Application of Weakly-Ionized Plasmas as Wing Flow-Control Devices,” AIAA Paper 2002-0350, Jan. 2002.

[3] Post, M. L., and Corke, T. C., “Separation Control on High Angle of Attack Airfoil Using Plasma Actuators,” *AIAA Journal*, Vol. 42, No. 11, Nov. 2004, pp. 2177–2184.
doi:10.2514/1.2929

[4] Post, M. L., and Corke, T. C., “Separation Control Using Plasma Actuators: Stationary and Oscillating Airfoils,” AIAA Paper 2004-0841, Jan. 2004.

[5] Corke, T. C., He, C., and Patel, M. P., “Plasma Flaps and Slats: An Application of Weakly-Ionized Plasma Actuators,” AIAA Paper 2004-2127, 2004.

[6] Post, M. L., and Corke, T. C., “Separation Control Using Plasma Actuators: Dynamic Stall Vortex Control on Oscillating Airfoil,” *AIAA Journal*, Vol. 44, No. 12, Dec. 2006, pp. 3125–3135.
doi:10.2514/1.22716

[7] Morris, S. C., Corke, T. C., VanNess, D., Stephens, J., and Douville, T., “Tip Clearance Control Using Plasma Actuators,” AIAA Paper 2005-0782, Jan. 2005.

[8] Thomas, F. O., Kozlov, A., and Corke, T. C., “Plasma Actuators for Landing Gear Noise Reduction,” AIAA Paper 2005-3010, May 2005.

[9] Thomas, F. O., Kozlov, A., and Corke, T. C., “Plasma Actuators for Bluff Body Flow Control,” AIAA Paper 2006-2845, June 2006.

[10] List, J., Byerley, A. R., McLaughlin, T. E., and Dyken, R. D., “Using a Plasma Actuator to Control Laminar Separation on a Linear Cascade Turbine Blade,” AIAA Paper 2003-1026, Jan. 2003.

[11] Huang, J., Corke, T. C., and Thomas, F. O., "Plasma Actuators for Separation Control of Low Pressure Turbine Blades," AIAA Paper 2003-1027, Jan. 2003.

[12] Corke, T. C., and Post, M. L., "Overview of Plasma Flow Control: Concepts, Optimization, and Applications," AIAA Paper 2005-0563, Jan. 2005.

[13] Huang, J., Corke, T. C., and Thomas, F. O., "Plasma Actuators for Separation Control of Low-Pressure Turbine Blades," *AIAA Journal*, Vol. 44, No. 1, Jan. 2006, pp. 51–57.
doi:10.2514/1.2903

[14] Huang, J., Corke, T. C., and Thomas, F. O., "Unsteady Plasma Actuators for Separation Control of Low-Pressure Turbine Blades," *AIAA Journal*, Vol. 44, No. 7, July 2006, pp. 1477–1487.
doi:10.2514/1.19243

[15] Patel, M. P., Ng, T. T., Vasudevan, S., Corke, T. C., and He, C., "Plasma Actuators for Hingeless Aerodynamic Control of an Unmanned Air Vehicle," AIAA Paper 2006-3495, June 2006.

[16] Visbal, M. R., Gaitonde, D. V., and Roy, S., "Control of Transitional and Turbulent Flows Using Plasma-Based Actuators," AIAA Paper 2006-3230, June 2006.

[17] Gaitonde, D. V., Visbal, M. R., and Roy, S., "Control of Flow Past a Wing Section with Plasma-Based Body Forces," AIAA Paper 2005-5302, June 2005.

[18] Visbal, M. R., and Gaitonde, D. V., "Control of Vortical Flows Using Simulated Plasma Actuators," AIAA Paper 2006-0505, Jan. 2005.

[19] Rizzetta, D. P., and Visbal, M. R., "Numerical Investigation of Plasma-Based Flow Control for Transitional Highly Loaded Low-Pressure Turbine," *AIAA Journal*, Vol. 45, No. 10, Oct. 2007, pp. 2554–2564.
doi:10.2514/1.29602

[20] Rizzetta, D. P., and Visbal, M. R., "Plasma-Based Flow Control Strategies for Transitional Highly Loaded Low-Pressure Turbines," *Journal of Fluids Engineering*, Vol. 130, No. 4, April 2008, Paper 041104.
doi:10.1115/1.2903816

[21] Rizzetta, D. P., and Visbal, M. R., "Large Eddy Simulation of Plasma-Based Control Strategies for Bluff Body Flow," *AIAA Journal*, Vol. 47, No. 3, March 2009, pp. 717–729.
doi:10.2514/1.39168

[22] Schatzman, D. M., and Thomas, F. O., "Turbulent Boundary Layer Separation Control with Plasma Actuators," AIAA Paper 2008-4199, June 2008.

[23] Vinokur, M., "Conservation Equations of Gasdynamics in Curvilinear Coordinate Systems," *Journal of Computational Physics*, Vol. 14, No. 2, Feb. 1974, pp. 105–226.
doi:10.1016/0021-9991(74)90008-4

[24] Steger, J. L., "Implicit Finite-Difference Simulation of Flow About Arbitrary Two-Dimensional Geometries," *AIAA Journal*, Vol. 16, No. 7, July 1978, pp. 679–686.
doi:10.2514/3.7377

[25] Roth, J. R., "Aerodynamic Flow Acceleration Using Paraelectric and Peristaltic Electrohydrodynamic Effects of a One Atmosphere Uniform Glow Discharge Plasma," *Physics of Plasmas*, Vol. 10, No. 5, May 2003, pp. 2117–2128.
doi:10.1063/1.1564823

[26] Roth, J. R., Sin, H., and Madham, R. C. M., "Flow Re-Attachment and Acceleration by Paraelectric and Peristaltic Electrohydrodynamic (EHD) Effects," AIAA Paper 2003-0531, Jan. 2003.

[27] Shyy, W., Jayaraman, B., and Anderson, A., "Modeling of Glow Discharge-Induced Fluid Dynamics," *Journal of Applied Physics*, Vol. 92, No. 11, Dec. 2002, pp. 6434–6443.
doi:10.1063/1.1515103

[28] Beam, R., and Warming, R., "An Implicit Factored Scheme for the Compressible Navier–Stokes Equations," *AIAA Journal*, Vol. 16, No. 4, April 1978, pp. 393–402.
doi:10.2514/3.60901

[29] Gordnier, R. E., and Visbal, M. R., "Numerical Simulation of Delta-Wing Roll," AIAA Paper 93-0554, Jan. 1993.

[30] Jameson, A., Schmidt, W., and Turkel, E., "Numerical Solutions of the Euler Equations by Finite Volume Methods Using Runge–Kutta Time Stepping Schemes," AIAA Paper 81-1259, June 1981.

[31] Pulliam, T. H., and Chaussee, D. S., "A Diagonal Form of an Implicit Approximate-Factorization Algorithm," *Journal of Computational Physics*, Vol. 39, No. 2, Feb. 1981, pp. 347–363.
doi:10.1016/0021-9991(81)90156-X

[32] Lele, S. A., "Compact Finite Difference Schemes with Spectral-Like Resolution," *Journal of Computational Physics*, Vol. 103, No. 1, Nov. 1992, pp. 16–42.
doi:10.1016/0021-9991(92)90324-R

[33] Visbal, M. R., and Gaitonde, D. V., "High-Order-Accurate Methods for Complex Unsteady Subsonic Flows," *AIAA Journal*, Vol. 37, No. 10, Oct. 1999, pp. 1231–1239.
doi:10.2514/2.591

[34] Gaitonde, D., Shang, J. S., and Young, J. L., "Practical Aspects of High-Order Accurate Finite-Volume Schemes for Electromagnetics," AIAA Paper 97-0363, Jan. 1997.

[35] Gaitonde, D., and Visbal, M. R., "High-Order Schemes for Navier–Stokes Equations: Algorithm and Implementation into FDL3DI," TR AFRL-VA-WP-TR-1998-3060, U.S. Air Force Research Laboratory, Wright-Patterson AFB, OH, Aug. 1998.

[36] Gordnier, R. E., "Computation of Delta-Wing Roll Maneuvers," *Journal of Aircraft*, Vol. 32, No. 3, May 1995, pp. 486–492.
doi:10.2514/3.46746

[37] Visbal, M. R., "Computational Study of Vortex Breakdown on a Pitching Delta Wing," AIAA Paper 93-2974, July 1993.

[38] Visbal, M., Gaitonde, D., and Gogineni, S., "Direct Numerical Simulation of a Forced Transitional Plane Wall Jet," AIAA Paper 98-2643, June 1998.

[39] Rizzetta, D. P., Visbal, M. R., and Stanek, M. J., "Numerical Investigation of Synthetic-Jet Flowfields," *AIAA Journal*, Vol. 37, No. 8, Aug. 1999, pp. 919–927.
doi:10.2514/2.811

[40] Rizzetta, D. P., and Visbal, M. R., "Direct Numerical Simulation of Flow Past an Array of Distributed Roughness Elements," AIAA Paper 2006-3527, June 2006.

[41] Rizzetta, D. P., and Visbal, M. R., "Numerical Investigation of Transitional Flow Through a Low-Pressure Turbine Cascade," AIAA Paper 2003-3587, June 2003.

[42] Rizzetta, D. P., Visbal, M. R., and Blaisdell, G. A., "A Time-Implicit High-Order Compact Differencing and Filtering Scheme for Large-Eddy Simulation," *International Journal for Numerical Methods in Fluids*, Vol. 42, No. 6, June 2003, pp. 665–693.
doi:10.1002/fld.551

[43] Rizzetta, D. P., and Visbal, M. R., "Application of Large-Eddy Simulation to Supersonic Compression Ramps," *AIAA Journal*, Vol. 40, No. 8, Aug. 2002, pp. 1574–1581.
doi:10.2514/2.1826

[44] Rizzetta, D. P., and Visbal, M. R., "Large-Eddy Simulation of Supersonic Cavity Flowfields Including Flow Control," *AIAA Journal*, Vol. 41, No. 8, Aug. 2003, pp. 1452–1462.
doi:10.2514/2.2128

[45] Visbal, M. R., and Rizzetta, D. P., "Large-Eddy Simulation on Curvilinear Grids Using Compact Differencing and Filtering Schemes," *Journal of Fluids Engineering*, Vol. 124, No. 4, Dec. 2002, pp. 836–847.
doi:10.1115/1.1517564

[46] Visbal, M. R., Morgan, P. E., and Rizzetta, D. P., "An Implicit LES Approach Based on High-Order Compact Differencing and Filtering Schemes," AIAA Paper 2003-4098, June 2003.

[47] Fureby, C., and Grinstein, F. F., "Monotonically Integrated Large Eddy Simulation," *AIAA Journal*, Vol. 37, No. 5, May 1999, pp. 544–556.
doi:10.2514/2.772

[48] Stoltz, S., and Adams, N. A., "An Approximate Deconvolution Procedure for Large-Eddy Simulation," *Physics of Fluids*, Vol. 11, No. 7, July 1999, pp. 1699–1701.
doi:10.1063/1.869867

[49] Mathew, J., Lechner, R., Foysi, H., Sesterhenn, J., and Friedrich, R., "An Explicit Filtering Method for Large Eddy Simulation of Compressible Flows," *Physics of Fluids*, Vol. 15, No. 8, Aug. 2003, pp. 2279–2289.
doi:10.1063/1.1586271.

[50] Rizzetta, D. P., and Visbal, M. R., "Numerical Study of Active Flow Control for a Transitional Highly-Loaded Low-Pressure Turbine," *Journal of Fluids Engineering*, Vol. 128, No. 5, Sep. 2006, pp. 956–967.
doi:10.1115/1.2238877

[51] Piomelli, U., and Balaras, E., "Wall-Layer Models for Large-Eddy Simulations," *Annual Review of Fluid Mechanics*, Vol. 34, No. 1, Jan. 2002, pp. 349–374.
doi:10.1146/annurev.fluid.34.082901.144919

[52] Visbal, M. R., and Gaitonde, D. V., "Very High-Order Spatially Implicit Schemes for Computational Acoustics on Curvilinear Meshes," *Journal of Computational Acoustics*, Vol. 9, No. 4, Dec. 2001, pp. 1259–1286.
doi:10.1142/s0218396x01000541

[53] Choi, H., and Moin, P., "Effects of the Computational Time Step on Numerical Solutions of Turbulent Flow," *Journal of Computational Physics*, Vol. 113, No. 1, July 1994, pp. 1–4.

doi:10.1006/jcph.1994.1112

[54] Sherer, S. E., Visbal, M. R., and Galbraith, M. C., “Automated Preprocessing Tools for Use with a High-Order Overset-Grid Algorithm,” AIAA Paper 2006-1147, Jan. 2006.

[55] Message Passing Interface Forum, “MPI: A Message-Passing Interface Standard,” Computer Science Dept. TR CS-94-230, Univ. of Tennessee, Knoxville, TN, April 1994.

[56] Ghosal, S., “Mathematical and Physical Constraints on Large-Eddy Simulation of Turbulence,” *AIAA Journal*, Vol. 37, No. 4, April 1999, pp. 425–433.
doi:10.2514/2.752

P. Givi
Associate Editor